GEOPHYSICS, VOL. 71, NO. 4 (JULY-AUGUST 2006); P. F101–F119, 20 FIGS., 6 TABLES.
10.1190/1.2213358

Petrophysical inversion of borehole array-induction logs: Part I — Numerical examples

Faruk O. Alpak[1], Carlos Torres-Verdín[2], and Tarek M. Habashy[3]

ABSTRACT

We have developed a new methodology for the quantitative petrophysical evaluation of borehole array-induction measurements. The methodology is based on the time evolution of the spatial distributions of fluid saturation and salt concentration attributed to mud-filtrate invasion. We use a rigorous formulation to account for the physics of fluid displacement in porous media resulting from water-base mud filtrate invading hydrocarbon-bearing rock formations. Borehole array-induction measurements are simulated in a coupled mode with the physics of fluid flow. We use inversion to estimate parametric 1D distributions of permeability and porosity that honor the measured array-induction logs. As a byproduct, the inversion yields 2D (axial-symmetric) spatial distributions of aqueous phase saturation, salt concentration, and electrical resistivity. We conduct numerical inversion experiments using noisy synthetic wireline logs. The inversion requires a priori knowledge of several mud, petrophysical, and fluid parameters. We perform a systematic study of the accuracy and reliability of the estimated values of porosity and permeability when knowledge of such parameters is uncertain. For the numerical cases considered in this paper, inversion results indicate that borehole electromagnetic-induction logs with multiple radial lengths of investigation (array-induction logs) enable the accurate and reliable estimation of layer-by-layer absolute permeability and porosity. The accuracy of the estimated values of porosity and permeability is higher than 95% in the presence of 5% measurement noise and 10% uncertainty in rock-fluid and mud parameters. However, for cases of deep invasion beyond the radial length of investigation of array-induction logging tools, the estimation of permeability becomes unreliable. We emphasize the importance of a sensitivity study prior to inversion to rule out potential biases in estimating permeability resulting from uncertain knowledge about rock-fluid and mud properties.

INTRODUCTION

Robust and accurate determination of fluid-flow related petrophysical parameters from borehole measurements is a fundamental objective of quantitative geophysical exploration. Geoelectrical measurements are sensitive to the spatial distributions of porosity, fluid saturation, and salt concentration. Therefore, it is reasonable to hypothesize that incorporating the physics of fluid flow in porous media into the analysis of geoelectrical borehole measurements will significantly improve current interpretation algorithms based solely on the estimation of electrical resistivity.

The phenomena of multiphase fluid flow and electromagnetic induction in porous media can be linked readily by means of an appropriate saturation equation when a priori information is available about the properties of the flowing fluids (i.e., viscosity, density, compressibility). Two-phase (or, occasionally, three-phase) multicomponent fluid displacement, which takes place during mud-filtrate invasion, provides a basis for the quantitative petrophysical interpretation of electrical conductivity around the wellbore. Tobola and Holditch (1991), and Yao and Holditch (1996) successfully used a history matching method based on time-lapse array-induction logs to estimate absolute permeability for the case of water-base mud filtrate invading low-permeability gas formations. Semmelbeck et al. (1995) attempted to estimate absolute permeability for low-permeability gas sands from array-induction measurements. Dussan et al. (1994) advanced a similar procedure to estimate vertical formation permeability using forward modeling and experimental data. Ramakrishnan and Wilkinson (1997, 1999) developed a method to esti-

Manuscript received by the Editor September 17, 2004; revised manuscript received December 6, 2005; published online August 15, 2006.
[1]Formerly Department of Petroleum and Geosystems Engineering, University of Texas at Austin, University Station, Mail Stop C0300, Austin, Texas 78712; presently Shell International E & P, 3737 Bellaire Boulevard, P. O. Box 481, Houston, Texas 77001. E-mail: omer.alpak@shell.com.
[2]Department of Petroleum and Geosystems Engineering, University of Texas at Austin, University Station, Mail Stop C0300, Austin, Texas 78712. E-mail: cverdin@uts.cc.utexas.edu.
[3]Schlumberger-Doll Research, Mathematics and Modeling Department, 36 Old Quarry Road, Ridgefield, Connecticut 06877. E-mail: thebashy@ridgefield.oilfield.slb.com.

mate fractional flow curves from radial profiles of electrical conductivity around the wellbore invoking the physics of fluid flow. Epov et al. (2002) inverted high-frequency electromagnetic logs to yield radial profiles of electrical resistivity and salt concentration consistent with two-phase hydrodynamic analysis of mud-filtrate invasion.

This paper introduces a stable, accurate, and efficient algorithm for the parametric petrophysical inversion of borehole array-induction logs. We introduce an inversion algorithm that estimates layer-by-layer fluid permeabilities and porosities of hydrocarbon-bearing formations. Inversion is posed as the minimization of a quadratic objective function subject to physical constraints on the unknown model parameters. We use a modification of the iterative Gauss-Newton technique to minimize the objective function. Each iterative step requires the solution of the forward problem. Numerical simulation of array-induction logs entails coupled simulations of mud-filtrate invasion and diffusive electromagnetic induction. We use efficient finite-difference algorithms to simulate fluid-flow and electromagnetic-induction phenomena. The simulations assume two-phase convective transport of three components, namely, oil/gas, water, and salt, to generate space- and time-domain distributions of aqueous phase saturation and salt concentration associated with water-base mud-filtrate invasion. Two-phase flow and electromagnetic-induction phenomena are coupled via Archie's saturation equation (Archie, 1942). This process also considers the process of salt mixing occurring within the aqueous phase as a result of contrasts of salt concentration between invading and in-situ fluids.

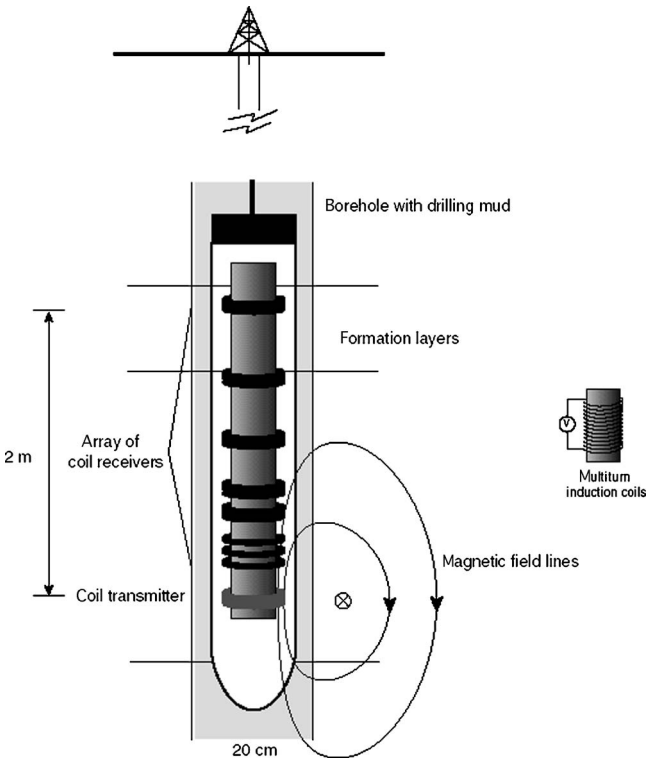

Figure 1. Simplified schematic description of the measurement principle of the array-induction imager tool (adapted from Blok and Oristaglio, 1995): A multiturn coil supporting a time-varying current generates a magnetic field that induces electrical currents in the surrounding rock formation. An array of receiver coils measures the magnetic field induced by both the source and the secondary rock-formation currents.

In part one of this two-part study, we introduce our methodology and present numerical examples for ideal single-well 2D axisymmetric near-borehole models. In a forthcoming paper, we will describe results of applying the methodology to field wireline array-induction logs.

The central component of this paper is a systematic sensitivity study for the simultaneous estimation of layer-by-layer absolute permeability and porosity from synthetically generated array-induction logs contaminated with various levels of additive Gaussian noise. For simplicity, from this point onward, we refer to the absolute fluid permeability of rock formations simply as permeability. We perform inversions for the cases where perturbations are made to the a priori information about rock and fluid properties. We give special consideration to the assumption of specific mud properties that determine the time evolution of mudcake growth and permeability and, consequently, the time evolution of flow rate of mud-filtrate invasion.

PETROPHYSICAL INVERSION OF ARRAY-INDUCTION LOGS

Our objective is to estimate layer-by-layer permeability and porosity from borehole array-induction logs. Measurements consist of the vertical component of the total magnetic field acquired at multiple receiver locations and frequencies (Figure 1). The forward model that couples borehole induction logs with fluid-flow phenomena is a nonlinear function of the spatial distribution of permeability, porosity, and other relevant rock and fluid properties. We assume the availability of saturation and pressure dependent rock and PVT-dependent fluid properties from ancillary wireline logs and laboratory experiments. Subsequently, we appraise this assumption with a sensitivity study in which we consider perturbations of a priori known parameters and quantify their influence on the estimations. Table 1 summarizes the underlying assumptions and associated qualitative uncertainty for the various parameters required by the petrophysical inversion technique that we develop in this paper.

Inversion algorithm

Inversion of layer-by-layer porosity and permeability values is posed as a minimization problem that involves a quadratic objective function subject to physical constraints (Torres-Verdín and Habashy, 1994). The objective function is given by,

$$C(\mathbf{x}) = \frac{1}{2}[\mu\{\|\mathbf{W}_d \cdot \mathbf{e}(\mathbf{x})\|^2 - \chi^2\} + \|\mathbf{W}_x \cdot (\mathbf{x} - \mathbf{x}_p)\|^2], \tag{1}$$

where $\mathbf{e}(\mathbf{x})$ is a vector whose jth element is the residual error (data mismatch) of the jth measurement. The residual error is the difference between the measured and numerically simulated logs, given by

$$\mathbf{e}(\mathbf{x}) = [(S_1(\mathbf{x}) - m_1), \ldots, (S_M(\mathbf{x}) - m_M)]^T = \mathbf{S}(\mathbf{x}) - \mathbf{m}, \tag{2}$$

where the superscript T denotes the transpose, M is the number of measurements, and m_j denotes the entries of vector $\mathbf{m}$, which correspond to array-induction measurements indexed with respect to

depth location, source-receiver distance, and operating frequency. The entries of vector $\mathbf{S}$, S_j, correspond to the numerically simulated logs predicted by the vector of model parameters $\mathbf{x}$, given by

$$\mathbf{x} = [x_1, \ldots, x_N]^T = \mathbf{y} - \mathbf{y}_R, \quad (3)$$

where N is the number of unknowns. The vector of model parameters $\mathbf{x}$ is defined as the difference between the vector of the actual model parameters $\mathbf{y}$ and a reference model $\mathbf{y}_R$. All a priori information on the model parameters such as those derived from independent measurements is included in the reference model. The scalar factor $\mu(0 < \mu < \infty)$ is a regularization parameter (also called a Lagrange multiplier) that assigns relative importance to the two additive terms of the quadratic objective function. The choice of μ produces an estimate of $\mathbf{x}$ that has a finite, minimum weighted norm with respect to the prescribed model $\mathbf{x}_p$, and which globally misfits the measurements.

In equation 1, the second additive term of the objective function is included to stabilize the minimization problem. This term suppresses any possible magnification of errors in $\mathbf{x}$ because of measurement noise. The matrix $\mathbf{W}_x^T\mathbf{W}_x$ is the inverse of the model covariance matrix that represents the degree of confidence in the prescribed model $\mathbf{x}_p$, and $\mathbf{W}_d^T\mathbf{W}_d$ is the inverse of the data covariance matrix describing the estimated uncertainties in the measurements because of noise

Table 1. Summary of geometrical, mud, and petrophysical properties assumed in the petrophysical inversion algorithm developed in this paper. Each parameter is described by both the specific type of assumption concerning its origin and the associated qualitative uncertainty in the estimation of porosity and permeability from array-induction logs.

Parameter	Unit	Type	Uncertainty
Mudcake permeability	(mD)	A priori	Low
Mudcake porosity	(fraction)	A priori	Low
Mud solid fraction	(fraction)	A priori	Low
Mudcake maximum thickness	(cm)	A priori	Medium
Formation rock compressibility	(kPa^{-1})	A priori	Low
Aqueous phase viscosity (mud filtrate)	(Pa.s)	A priori	Low
Aqueous phase density (mud filtrate)	(g/cm^3)	A priori	Low
Aqueous phase formation volume factor (mud filtrate)	($res.m^3/std.m^3$)	A priori	Low
Aqueous phase compressibility (mud filtrate)	(kPa^{-1})	A priori	Low
Oleic/gaseous phase viscosity	(Pa.s)	A priori	Medium
Oleic/gaseous phase API density	(°API)	A priori	Medium
Oleic/gaseous phase density	(g/cm^3)	A priori	Medium
Oleic/gaseous phase formation volume factor	($res.m^3/std.m^3$)	A priori	Medium
Oleic/gaseous phase compressibility	(kPa^{-1})	A priori	Medium
Formation pressure at the formation top (at the reference depth = 0 m)	(MPa)	A priori	Medium
Mud hydrostatic pressure	(MPa)	A priori	Low
Wellbore radius	(m)	A priori	Low
Formation outer boundary location	(m)	A priori	Low
Formation temperature	(°C)	A priori	Low
a-constant in the Archie's equation	(dimensionless)	A priori	Medium
m-cementation exponent in the Archie's equation	(dimensionless)	A priori	Medium/high
n-aqueous phase saturation exponent in the Archie's equation	(dimensionless)	A priori	Medium/high
Mud conductivity	(mS/m)	A priori	Low
Upper and lower shoulder bed conductivities	(mS/m)	A priori	Medium
Logging interval used for inversion	(m)	A priori	NA
Relative permeability function	(dimensionless)	A priori	Medium/high
Capillary pressure function	(Pa)	A priori	Medium/high
Initial aqueous phase saturation of the formation	(fraction)	A priori	Medium/high
Layer thicknesses	(m)	A priori/1D inversion	Low/NA
Layer permeabilities	(mD)	Inversion	NA
Layer porosity	(fraction)	Inversion	NA

contamination. We employ the following form of the data residual vector with the purpose of putting the various measurements on equal footing:

$$\|\mathbf{W}_d \cdot \mathbf{e}(\mathbf{x})\|^2 = \sum_{j=1}^{M} w_j \left| \frac{S_j(\mathbf{x})}{m_j} - 1 \right|^2. \quad (4)$$

Moreover, the variable χ^2 in equation 1 is the expected measure of weighted data misfit computed with equation 4. This variable is assumed known a priori from the estimated signal-to-noise ratio of the measurements. The inversion will stop when the weighted data misfit computed with equation 4 reaches the value of χ^2.

In equation 1, the vector of model parameters $\mathbf{x}$ is constructed with the layer-by-layer values of permeability and porosity. Figure 2 describes the model-domain parameterization. We assume that locations of layer boundaries are available from other types of logs, such as high-resolution resistivity logs or borehole images. An arbitrary combination of the above mentioned petrophysical parameters could be included in vector $\mathbf{x}$.

To solve the nonlinear inverse problem, we employ a modification of the Gauss-Newton minimization method. The inverted model parameters $\mathbf{x}$ are constrained to remain within their physical bounds using a nonlinear transformation (Habashy and Abubakar, 2004). A backtracking line-search algorithm is used along the descent direction to guarantee a reduction of the objective function from iteration to iteration. The choice of the Lagrange multiplier is adaptively linked to the condition number of the Hessian matrix of the objective function. We progressively increase the weight of the data misfit term in the objective function with respect to the stabilization term as the inversion algorithm iterates toward the minimum.

Evaluating the Hessian matrix is the most computationally intensive part of the inversion. We employ four alternative approximate strategies for computing the Hessian matrix to accelerate the inversion: Broyden symmetric rank-one, Powell-Symmetric-Broyden (PSB) rank-two, Davidson-Fletcher-Powell (DFP) rank-two, and Broyden-Fletcher-Goldfarb-Shanno (BFGS) rank-two update methods (Gill et al., 1981).

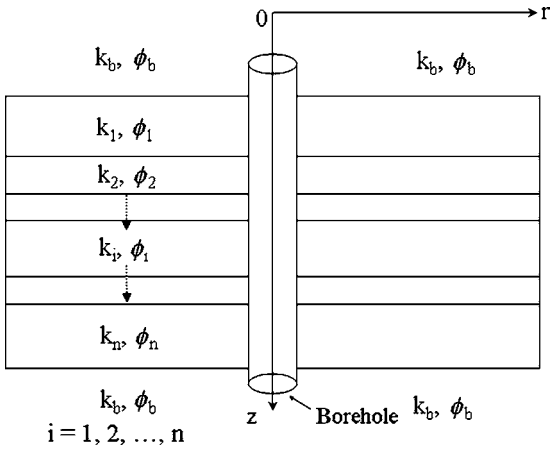

Figure 2. Model parameterization with homogeneous and isotropic horizontal geologic layers. Model parameters are layer-by-layer permeabilities and porosities denoted by k and ϕ, respectively.

Computing the rate of mud-filtrate invasion

We use the general numerical algorithm INVADE to simulate the process of mud-filtrate invasion in vertical boreholes (Delshad et al., 1996; Wu et al., 2001; Wu et al., 2005). Simulations with INVADE yield an equivalent time-domain mud-filtrate flow-rate function. This function replicates the time evolution of mudcake growth. Because clay platelets form mudcake with permeabilities on the order of 1×10^{-3} mD, the rate of mud-filtrate invasion is often controlled by mudcake, with marginal influence of formation permeability. Extensive simulations conducted with INVADE agree with this observation. We impose the numerically computed invasion rate as a local source condition (flux as a function of depth) to simulate fluid displacement and salt mixing in the invaded rock formation. This procedure allows us to readily incorporate the physics of mud-filtrate invasion into an algorithm that couples the simulation of multiphase fluid flow in porous media with the simulation of borehole array-induction logs.

Forward model of the petrophysical inversion algorithm

Time and space distributions of aqueous phase saturation and salt concentration are modeled as convective transport of hydrocarbon and aqueous phases and hydrocarbon. Ions are assumed to be soluble only within the aqueous phase and lumped into a single salt component. In the forward problem, we assume a salt concentration contrast between the in-situ formation brine and the invading mud-filtrate. According to Ramakrishnan and Wilkinson (1997) diffusion has only a small effect at invasion-radius length scales. In addition, equilibration of salt concentration among pores occurs at time scales shorter than the invasion time scale, whereupon local-level aqueous phase salt concentrations remain the same from pore to pore. Therefore, we only consider convective miscible salt transport within the aqueous phase and neglect diffusional spreading of the interface between mud-filtrate and formation brine.

We perform numerical modeling with a finite-difference based near-borehole fluid-flow simulator formulated in cylindrical coordinates (Aziz and Settari, 1979). The simulations yield time and space distributions of aqueous phase saturation (S_w) and salt concentration (C_w) attributable to mud-filtrate invasion. We assume that salt is only soluble in the aqueous phase. We simulate convective salt transport after a converged solution for the time-step has been found and the interblock flows are determined. We invoke mass conservation to update the spatial distribution of salt concentration.

Spatial distributions of aqueous phase saturation for a given logging time are subsequently transformed into spatial distributions of electrical conductivity using Archie's equation (Archie, 1942),

$$\sigma(\mathbf{r}) = \frac{\sigma_w(\mathbf{r})\phi^m(\mathbf{r})S_w^n(\mathbf{r})}{a}, \quad (5)$$

applied gridblock-by-gridblock in the simulation grid. In the above equation, the vector $\mathbf{r}$ designates spatial location, and the quantities $\sigma(\mathbf{r})$, $\sigma_w(\mathbf{r})$, and $S_w(\mathbf{r})$ denote spatial distributions of formation conductivity, brine conductivity, and aqueous phase saturation, respectively. Cementation and saturation exponents m and n, respectively, and the tortuosity/cementation coefficient a are empirical constants measured on rock-core samples.

Spatial distributions of brine conductivity are computed gridblock-by-gridblock from the simulated salt concentrations using the following transformation (Zhang et al., 1999):

$$\sigma_w(\mathbf{r}) = \left[\left(0.0123 + \frac{3647.5}{C_w^{0.955}(\mathbf{r})}\right)\frac{82}{1.8T + 39}\right]^{-1}, \quad (6)$$

where $C_w(\mathbf{r})$ and T stand for the spatial distribution of aqueous phase salt concentration (ppm) and uniform formation temperature (°C), respectively. The brine conductivity model assumes instantaneous temperature equilibrium between invading and in-situ aqueous phases. Our choices of saturation equation and brine conductivity transform strictly depend on the specific properties of the formation under consideration. We assume that the reservoir rock consists predominantly of clean sands, and therefore, that Archie's equation and the aforementioned brine conductivity transform accurately describe the rock's effective electrical conductivity. Presence of substantial amounts of dispersed, structural, or laminated clay would entail the use of other types of petrophysical relationships between water saturation and electrical conductivity.

Forward modeling of array-induction logs is accomplished by solving quasi-static Maxwell's equations in the frequency domain. This approach provides the following equation for the electric field **E**:

$$\sigma^{-1}\,\nabla\,\times\,\nabla\,\times\,\mathbf{E} - i\omega\mu\mathbf{E} = i\omega\mu\sigma^{-1}\mathbf{J}_S, \quad (7a)$$

where the symbols σ, ω, μ, and $\mathbf{J}_S$ denote electrical conductivity (S/m), angular frequency (radians/s), magnetic permeability constant (H/m), and impressed (source) electric current density (A/m^2), respectively, with $i = \sqrt{-1}$, and $e^{-i\omega t}$ as the assumed time (t [s]) variation. We solve equation 7a with a finite-difference algorithm implemented on a staggered grid (Druskin and Knizhnerman, 1999). The induced magnetic field **B** at the receiver coils is calculated explicitly from the equation

$$\mathbf{B} = (i\omega)^{-1}\,\nabla\,\times\,\mathbf{E}. \quad (7b)$$

NUMERICAL SENSITIVITY STUDY

General considerations

The synthetic model, shown in Figure 3, consists of a vertical borehole that penetrates a hydrocarbon-bearing formation composed of three permeable isotropic and homogeneous horizontal layers with sealing upper and lower shoulder beds. We assume that the reservoir is buried in a shale background and that upper, lower, and outer domain boundaries exhibit no-flow conditions. The lateral reservoir boundary is 300 m away from the borehole axis. From the onset of drilling, the permeable formation is subject to water-base mud filtrate invasion. We consider the acquisition of wireline array-induction logs vertically across the formation at a specific logging time after the onset of invasion. The wireline sonde is the array-induction imager tool described in Figure 1, which includes multiple source-receiver configurations and operating frequencies (Hunka et al., 1990). Such a measurement configuration ensures multiple radial lengths of investigation (Barber and Rosthal, 1991).

We list specific mud, mudcake, formation fluid and rock properties, and further details of the acquisition geometry in Table 2. We implement a 141 × 30 grid in the radial-vertical cylindrical coordinate system to simulate the process of mud filtrate invasion. The grid is uniform in the vertical direction whereas block sizes increase logarithmically in the radial direction away from the wellbore.

Layer-by-layer relative permeability and capillary pressure functions are illustrated in Figure 4a and b. The spatial distribution of initial aqueous and oleic phase saturation is derived from the hydrodynamic equilibrium state for the uninvaded formation of interest. Figure 4c shows the averaged mud-filtrate invasion history that is imposed on the fluid-flow simulator as the source condition. Rate history, simulated with `INVADE`, is transformed into an equivalent single-step rate schedule via integral averaging that maintains volumetric balance. In this case, the early-time rate transient is short-lived in comparison to the stabilized rate; therefore, the averaged rate of invasion remains very close to the stabilized rate. This result also justifies the use of the single-step, equal-volume average rate. As shown in Figure 4c, the flow rate resulting from removal of mudcake attributable to drill-string trip-out (ruboff) at the logging time (1.5th day) also is incorporated into the time history of mud-filtrate invasion. The postruboff average invasion rate is computed using the same averaging approach as in the case of preruboff average rate. Simulated measurements are contaminated with zero-mean additive Gaussian random noise. The standard deviation of the additive synthetic random noise is varied between 1% and 21%, depending on the inversion study of interest. In this paper, we define the standard deviation of synthetic noise as a percentage of the absolute value of the individual measurement under consideration. Unless otherwise stated, for numerical inversion examples, we use a slightly coarser numerical mesh of size 121 × 30 in the radial and vertical directions, respectively. Electromagnetic fields computed with a 141 × 30 and a 121 × 30 mesh are within 0.1% of each other.

Spatial distributions of aqueous phase saturation, salt concentration, and electrical conductivity

We consider the invasion of water-base mud into hydrocarbon-bearing formations wherein the salinity of the in-situ brine is higher

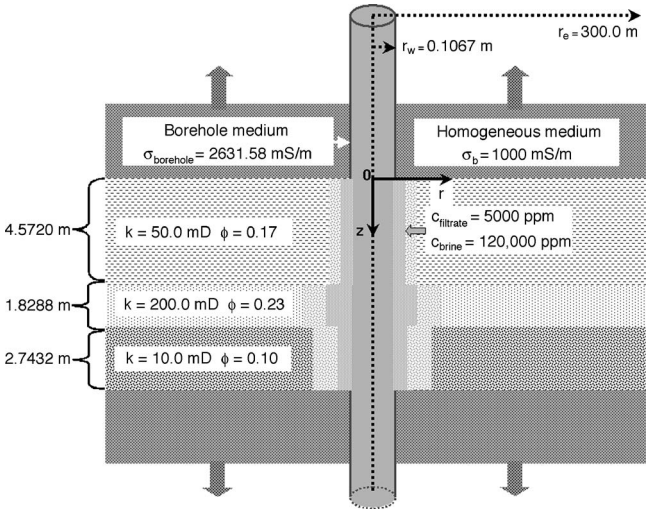

Figure 3. Synthetic rock-formation model for the sensitivity study. Two-dimensional vertical cross section of the permeable rock formation penetrated by a vertical borehole. The three-layer formation is subject to water-base mud-filtrate invasion.

Table 2. Summary of geometrical, petrophysical, mudcake, fluid, and sensor parameters associated with the reservoir model used in the numerical sensitivity study.

Variable	Unit	Value
Mudcake permeability	(mD)	0.010
Mudcake porosity	(fraction)	0.400
Mud solid fraction	(fraction)	0.500
Mudcake maximum thickness	(cm)	1.270
Formation rock compressibility	(kPa^{-1})	7.252×10^{-10}
Aqueous phase viscosity (mud filtrate)	(Pa.s)	1.274×10^{-3}
Aqueous phase density (mud filtrate)	(g/cm^3)	1.001
Aqueous phase formation volume factor (mud filtrate)	($res.m^3/std.m^3$)	0.996
Aqueous phase compressibility (mud filtrate)	(kPa^{-1})	3.698×10^{-7}
Oleic phase viscosity	(Pa.s)	3.550×10^{-4}
Oleic phase API density	(°API)	42
Oleic phase density	(g/cm^3)	0.816
Oleic phase formation volume factor	($res.m^3/std.m^3$)	1.471
Oleic phase compressibility	(kPa^{-1})	2.762×10^{-6}
Viscosity ratio (water to oil)	(dimensionless)	3.589
Formation pressure at the formation top (at the reference depth = 0 m)	(MPa)	20.684
Mud hydrostatic pressure	(MPa)	24.821
Wellbore radius	(m)	0.108
Formation outer boundary location	(m)	300.000
Formation temperature	(°C)	104.444
a-constant in the Archie's equation	(dimensionless)	1.000
m-cementation exponent in the Archie's equation	(dimensionless)	2.000
n-aqueous phase saturation exponent in the Archie's equation	(dimensionless)	2.000
Mud conductivity	(mS/m)	2631.579
Upper and lower shoulder bed conductivities	(mS/m)	1000.000
Logging interval used for inversion	(m)	6.096×10^{-1}

than that of mud filtrate. Mud filtrate has a salt concentration of 5,000 ppm, whereas the in-situ brine has 120,000 ppm of salt. The near-borehole oleic phase saturation and salt concentration distributions for the 1.5th and 3rd day of mud-filtrate invasion can also be viewed as the spatial distribution of near-borehole aqueous phase saturation (Figure 5), because the saturation relationship $S_w(\mathbf{r}) = 1 - S_o(\mathbf{r})$ holds for the two-phase immiscible flow of aqueous and oleic phases. Figure 6 shows snapshots of the time evolution of the spatial distribution of electrical conductivity for the 1.5th, 3rd, 4.5th, 8.5th, and 12th day after the onset of mud-filtrate invasion. These electrical conductivity snapshots are calculated from the spatial distributions of aqueous phase saturation and salt concentration using equations 5 and 6.

In our numerical simulations, invasion of water-base mud filtrate into a hydrocarbon-bearing zone containing irreducible brine (with salt concentration much higher than that of mud filtrate) is responsible for the presence of a conductive annulus zone (Dumanoir et al., 1957; Ramakrishnan and Wilkinson, 1997; and Zhang et al., 1999). This observation is consistent with results described by George et al. (2004).

Borehole array-induction measurements

Figure 7 shows the apparent electrical conductivity logs simulated for the 1.5th, 3rd, 4.5th, 8.5th, and 12th day after the onset of mud-filtrate invasion. At relatively early stages of mud-filtrate invasion, the shallow investigating arrays (10-, 20-, and 30-in arrays) are more sensitive to time-dependent changes in the near-borehole conductivity distribution than are arrays with a deeper radial length of investigation (60- and 90-in arrays). As mud-filtrate invasion progresses, the deeply

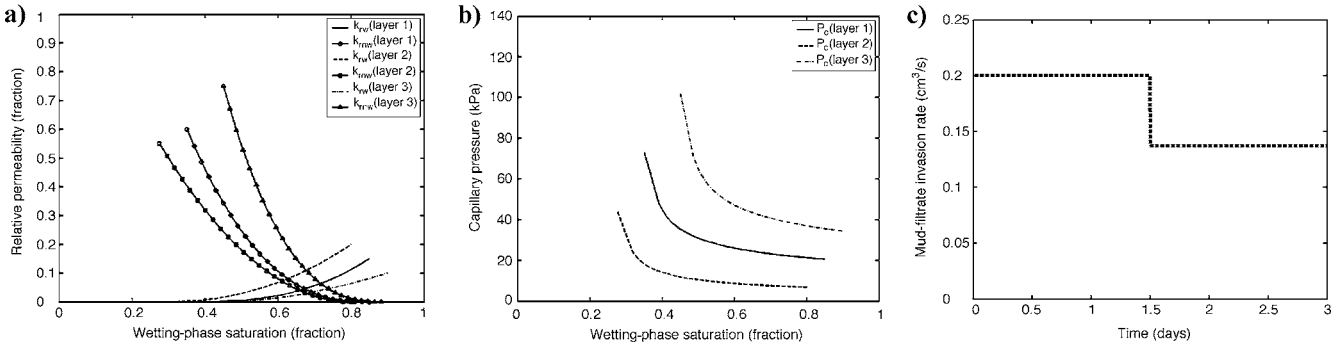

Figure 4. Layer-by-layer (a) relative permeability and (b) capillary pressure functions used in fluid-flow simulations for the synthetic rock-formation model considered in the sensitivity study. Relative permeability and capillary pressure saturation functions for each layer were generated using the modified Brooks-Corey model (see Table 5, actual value section). (c) Time average of the rate of mud-filtrate invasion for pre- and post-removal of mudcake.

sensing resistivity arrays exhibit enhanced sensitivity to the corresponding perturbation of electrical conductivity.

From the geologic point of view, the influence of mud-filtrate invasion on array-induction logs becomes more apparent across relatively more permeable beds. Fluid displacement occurs faster in high-permeability beds, leading both the phase saturation and salt concentration fronts. Consequently, the perturbation of electrical conductivity extends deeper into the reservoir.

The above observations are confirmed further by the time-lapse analysis of simulated apparent conductivity logs shown in Figure 8, where we compute the change of apparent conductivity from $t_{\log 1}$ to $t_{\log 2}$, i.e., $\Delta\sigma_{\text{app.}} = \sigma_{\text{app. t log 2}} - \sigma_{\text{app. t log 1}}$. Changes of log responses are shown for $t_{\log 1} = 1.5$ days and $t_{\log 2} = 3$ days, $t_{\log 2} = 4.5$ days, $t_{\log 2} = 8.5$ days, $t_{\log 2} = 12$ days in Figure 8a–d, respectively.

Inversions of noisy synthetic array-induction logs

Array-induction logs acquired at the 1.5th day of mud-filtrate invasion are inverted to yield layer-by-layer values of permeability and porosity. Saturation-dependent functions, saturation equation parameters, and PVT properties of the fluids

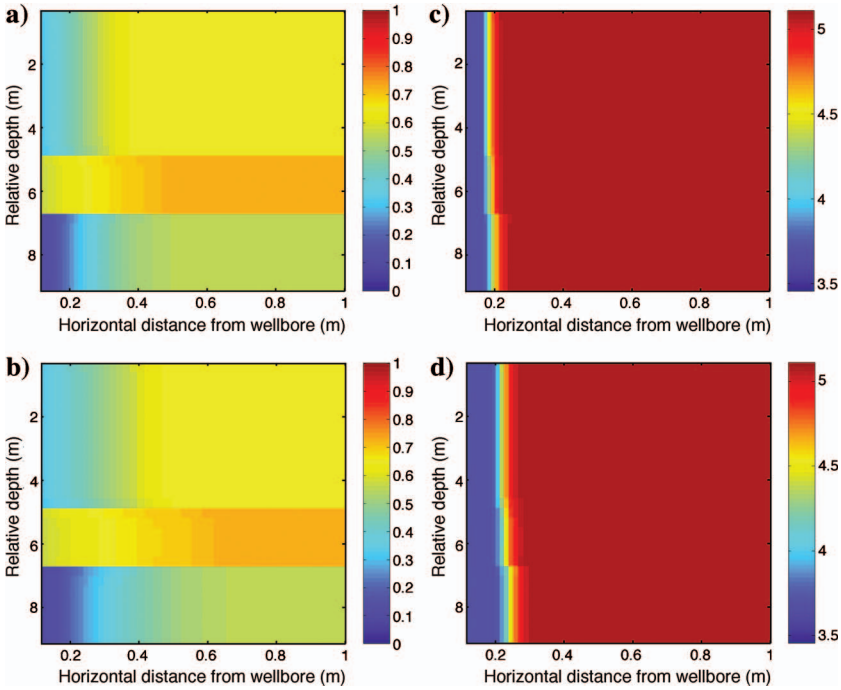

Figure 5. Spatial distributions of axisymmetric near borehole oleic phase saturation at various times after the onset of mud-filtrate invasion: (a) 1.5th day and (b) 3rd day. The spatial distribution of oleic-phase saturation $S_o(\mathbf{r}) = 1.0 - S_w(\mathbf{r})$ is shown in the units of pore volume fraction. Spatial distributions of salt concentration at the 1.5th and 3rd day of mud-filtrate invasion are shown in (c) and (d), respectively. Salt concentration is described in parts per million (ppm) using a logarithmic scale.

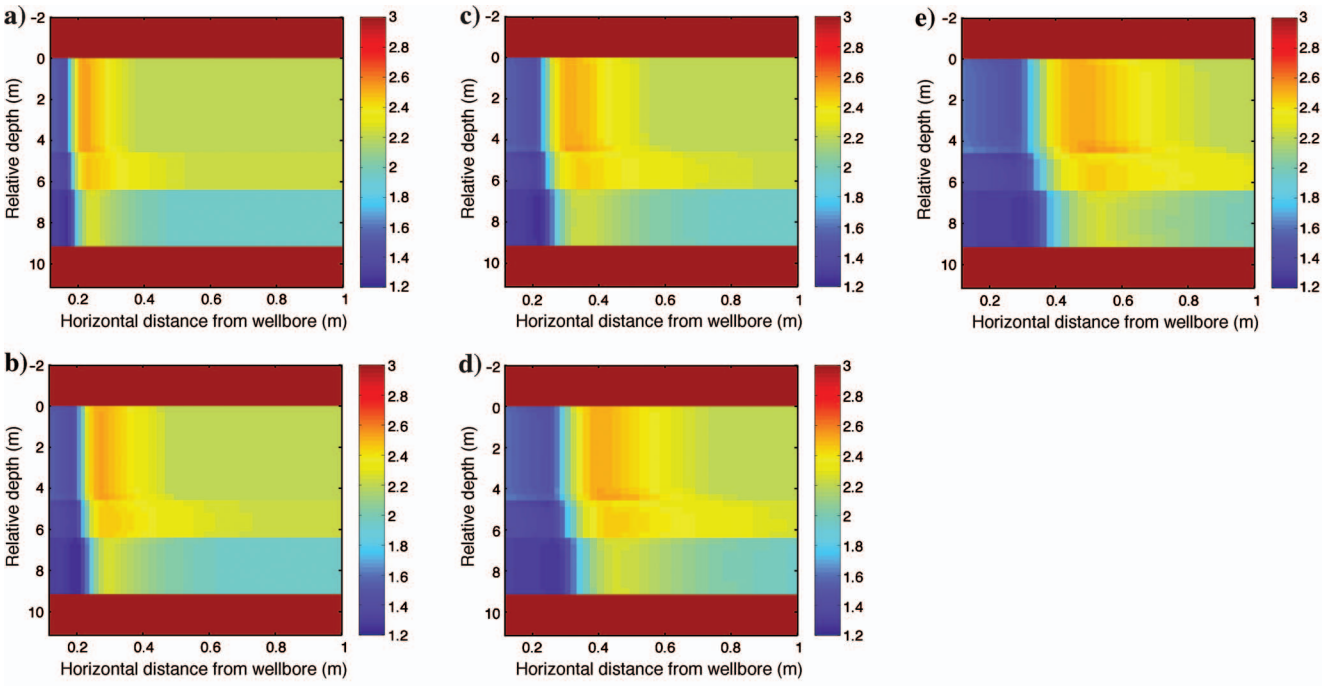

Figure 6. Snapshots of the spatial distribution of axisymmetric near borehole electrical conductivity for various times of mud-filtrate invasion after the onset of invasion: (a) 1.5th day, (b) 3rd day, (c) 4.5th day, (d) 8.5th day, and (e) 12th day. Electrical conductivities are shown with a logarithmic scale, i.e., $\log_{10}[\sigma(\mathbf{r})]$.

are assumed known from fluid samples and rock-core laboratory measurements.

Inversion results are presented together with true and initial-guess values. Uniform initial-guess values are chosen for both permeability and porosity. These uniform values are derived from the actual profiles by volumetrically averaging the true values of permeability and porosity, respectively. Figure 9a shows inversion results for permeability and Figure 9b displays inversion results for porosity. In this inversion example, synthetic measurements were contaminated with 3% additive zero-mean Gaussian noise.

We quantify the effect of the duration of mud filtrate invasion on the inverted values of permeability and porosity with the following set of results. Array-induction logs are simulated for acquisition times that correspond to the 4.5th and 12th day of mud-filtrate inva-

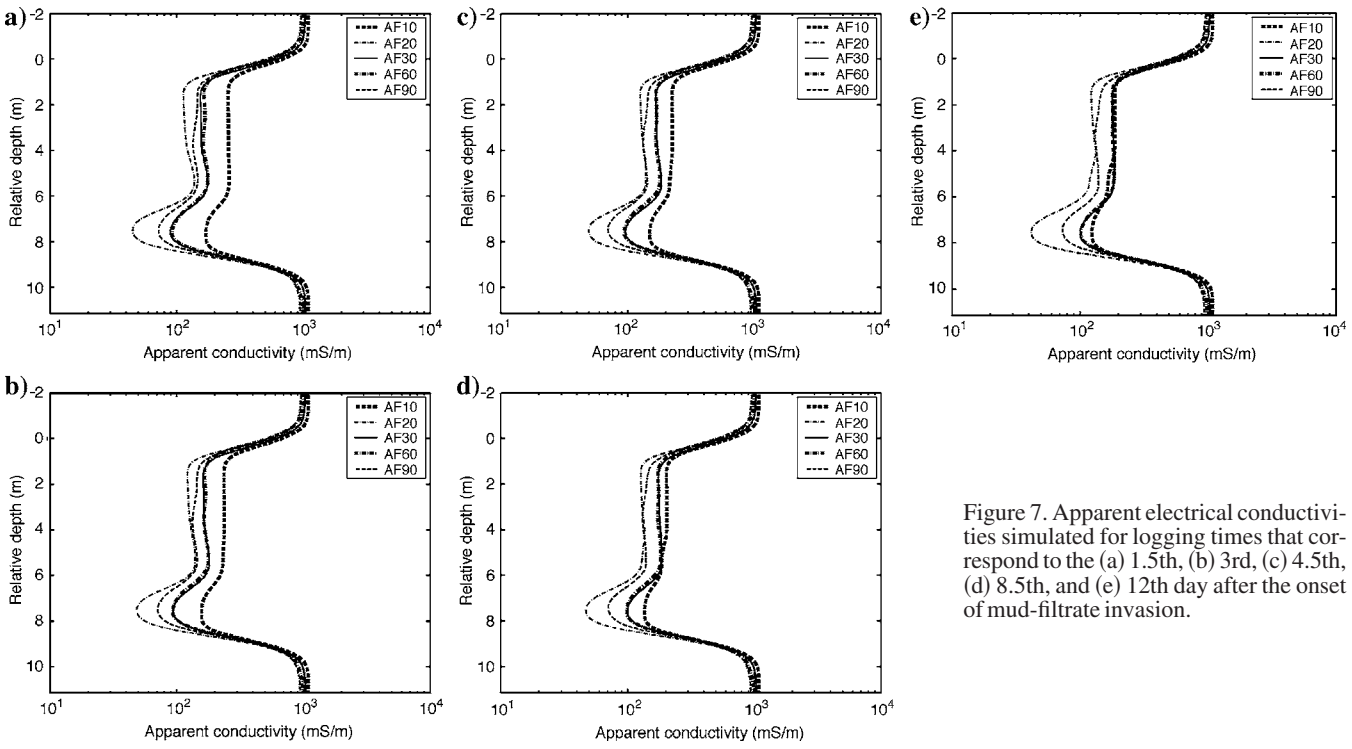

Figure 7. Apparent electrical conductivities simulated for logging times that correspond to the (a) 1.5th, (b) 3rd, (c) 4.5th, (d) 8.5th, and (e) 12th day after the onset of mud-filtrate invasion.

Figure 8. Change in apparent conductivity curves from $t_{\log 1}$ to $t_{\log 2}$, i.e., $\Delta\sigma_{\text{app.}} = \sigma_{\text{app. t log 2}} - \sigma_{\text{app. t log 1}}$, where $t_{\log 1} = 1.5$ day and (a) $t_{\log 2} = 3$, (b) 4.5, (c) 8.5, and (d) 12 day, respectively, after the onset of mud-filtrate invasion.

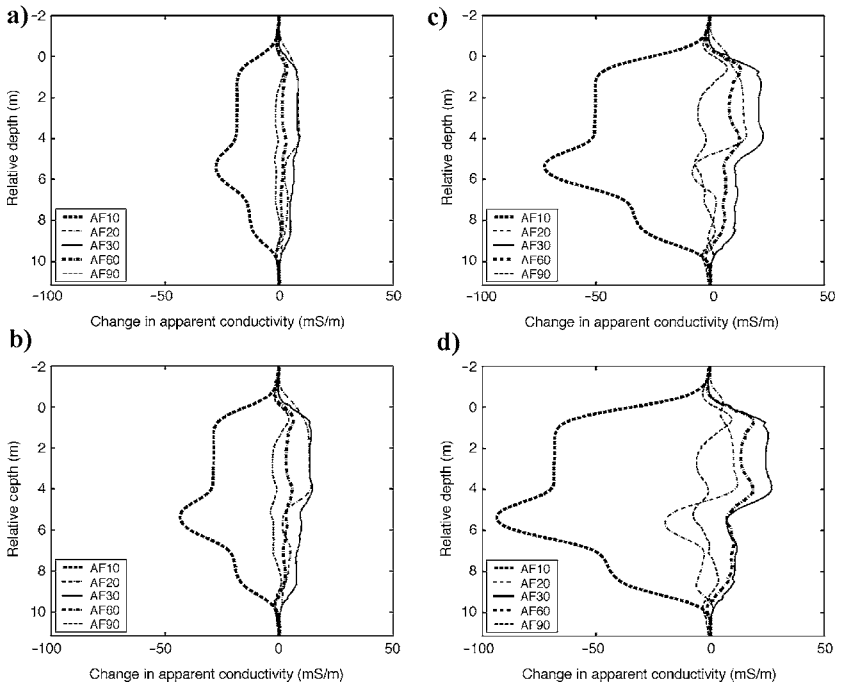

sion. For these cases, we extend the mud-filtrate invasion rate computed with INVADE for the preruboff invasion period shown in Figure 4c to the time of log acquisition. The simulated logs are contaminated with 3% additive Gaussian noise and input to the inversion algorithm. Initial guess values are the same as in the previous case. Inversion results for log-acquisition at the 4.5th day of invasion are shown in Figure 10a and b. Similar results are displayed in Figure 10c and d for the inversion of array-induction logs acquired at the 12th day of invasion. We note that the same inversion exercise can be interpreted from the viewpoint of the invasion rate while keeping the log-acquisition time constant. Specifically, measurements simulated 4.5 days after the onset of invasion are approximately equivalent to measurements simulated 1.5 days after the onset of invasion with an invasion rate equal to three times the original rate. Similarly, measurements simulated 12 days after the onset of invasion are approximately equivalent to measurements simulated 1.5 days after the onset of invasion with an invasion rate equal to eight times the original rate.

For the case of induction logs acquired 12 days after the onset of invasion, the inverted permeability and porosity values accurately match the actual values for all layers, despite the noisy measurements. The inversion exercises indicate that permeability values, estimated from measurements contaminated with 3% noise, consistently improve as the duration of invasion increases. An analysis of the time evolution of near-borehole electrical conductivity (Figure 6) together with simulated array-induction logs (Figure 7), and their time-lapse sensitivity (Figure 8) provide a quantitative explanation for this observation. Radial movement of the aqueous phase saturation and salt concentration fronts leads to radial variations of electrical conductivity. The time evolution of these fronts is highly conditioned by the rock's permeability. Thus, when the spatial variations of electrical conductivity are contained within the radial length of investigation of the array-induction imager tool, induction logs will remain sensitive to permeability.

Conversely, when the spatial variations of electrical conductivity are located deeper than the radial length of investigation of the array-induction imager tool, the sensitivity of induction logs to permeability will be negligible. On the other hand, all apparent conductivity logs with various radial lengths of investigation remain sensitive to porosity, regardless of the space-time evolution of the fluid saturation and salt concentration fronts. Array-induction logs will therefore exhibit a relatively higher degree of sensitivity to porosity than to permeability. Our numerical experiments consistently indicate an excellent reconstruction of porosity compared to the varying degrees of accuracy attained in the reconstruction of permeability.

Having established a physical insight to the time evolution of sensitivities of array-induction logs with respect to permeability and porosity, we select the logs simulated for the 12th day of mud-filtrate invasion, (or equivalently, for the 1.5th day of mud-filtrate invasion eight times the original rate of invasion) for the next numerical experiment. In this set of inversions, we contaminate the simulated logs with 3%, 5%, 8%, 12%, 15%, and 21% additive zero-mean Gaussian noise. To assess the sensitivity of the inversion to the choice of initial-guess values, we select a new set of uniform initial permeability and porosity values for these experiments. Figure 11a-l shows the outcome of the inversions for measurement-noise levels between 3% and 21%.

Inversions yield accurate reconstructions of permeability and porosity for 3% and 5% noise levels, despite the drastic change in initial-guess values. For 8% and 12% measurement-noise levels, the inverted permeability values deviate considerably from the true values. Estimated porosity values, however, remain unchanged with respect to the negative influence of measurement noise. However, from the 15% measurement-noise level onward, the inverted porosi-

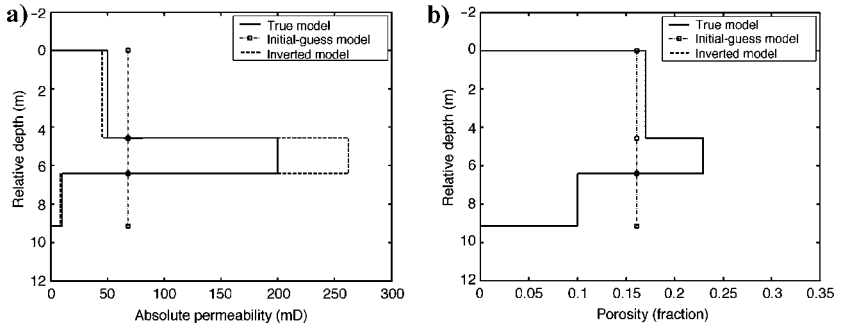

Figure 9. (a) Permeability and (b) porosity values inverted from induction logs acquired with the array-induction imager tool 1.5 days after the onset of mud-filtrate invasion. Inversion results are shown for the case of measurements contaminated with 3% zero-mean additive Gaussian noise.

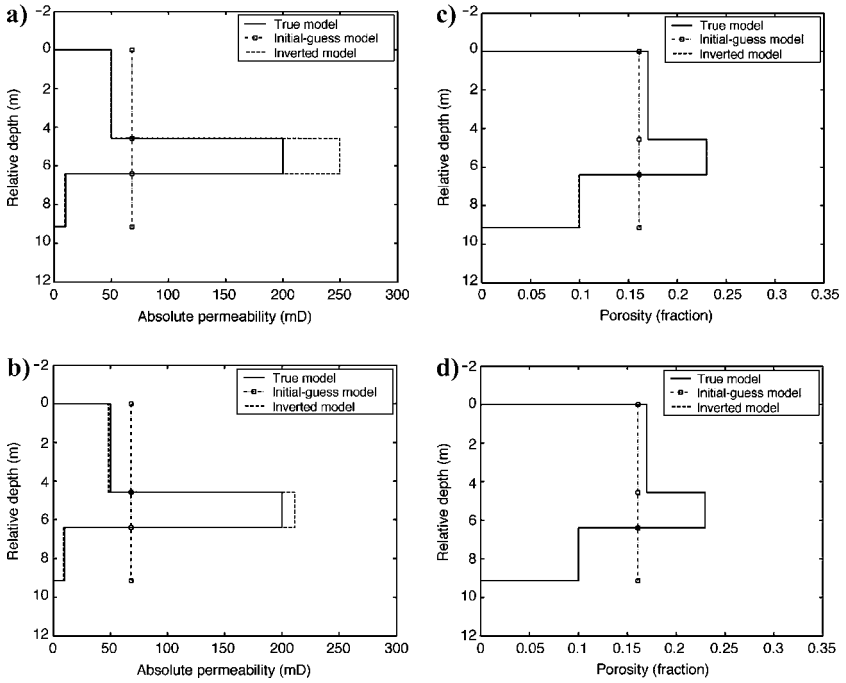

Figure 10. Permeability and porosity values inverted from induction logs acquired with the array-induction imager tool (a), (b) 4.5 days and (c), (d) and 12 days after the onset of mud-filtrate invasion. Inversion results are shown for the case of measurements contaminated with 3% zero-mean additive Gaussian noise.

ty values start to deviate from the true values. In general, at these very high noise levels, the accuracy of the estimated permeability is significantly poorer than that of porosity.

We quantify the uncertainty of the estimated values of porosity and permeability with the calculation of Cramer-Rao bounds using an approximation to the estimator's covariance matrix. The Cramer-Rao error bounds provide a probable range for a model parameter inverted from noisy measurements. Habashy and Abubakar (2004) detail the computation of these error bounds. The assumption underlying the approximate computation of the estimator's covariance matrix is that the errors in the measurements are random and Gaussian.

To appraise the uncertainty of inversion results, we select array-induction logs simulated for the 12th day of mud-filtrate invasion (or equivalently, for the 1.5th day of mud-filtrate invasion eight times the original rate of invasion). We corrupt the simulated measurements with 3% additive zero-mean Gaussian noise. Also, we use the

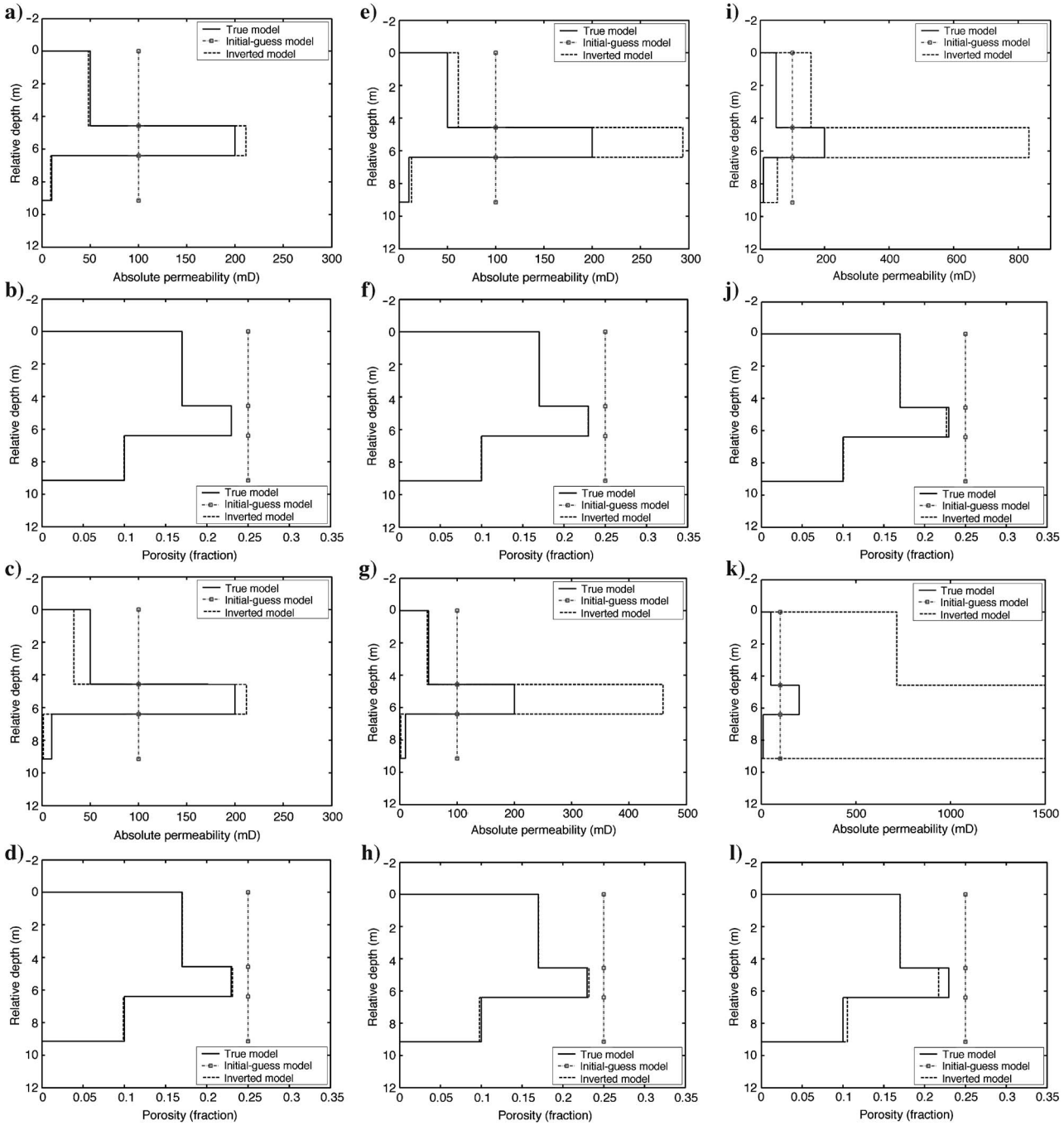

Figure 11. Permeability and porosity values inverted from induction logs acquired with the array-induction imager tool 12 days after the onset of mud-filtrate invasion. Inversion results are shown for the cases of measurements contaminated with 3%, 5%, 8%, 12%, 15%, and 21% zero-mean additive Gaussian noise in panels (a), (b); (c), (d); (e), (f); (g), (h); (i), (j); and (k), (l), respectively. In this example, initial-guess values are chosen far away from the volumetric mean values of permeability and porosity.

same finite-difference numerical mesh that was used to simulate the measurements (141×30) in order to prevent any systematic errors (although less than 1%) from affecting the outcome of the uncertainty analysis. Inverted values of permeability and porosity along with the computed upper and lower uncertainty bounds are shown in Figure 12a and b for the measurement-noise level of 3%. Inversion results indicate relatively small uncertainty bounds on the reconstructed model parameters. For some model parameters, the true value of the parameter falls outside the probable uncertainty bounds yielded by the inversion. The latter behavior is observed for the permeability associated with the middle layer. We note that bounds for porosity are lower than those for permeability.

For the same synthetic case described above, the numerically simulated array-induction log is used to invert permeability values only. In this case, the spatial porosity distribution is assumed known from other measurements such as density and neutron logs. Inverted values of permeability are shown along with error bounds and initial-guess values in Figure 13 for the measurement-noise level of 3%. Estimated permeability values are comparable to those obtained with the simultaneous inversion approach. We note that for the independent inversion of permeability, a priori knowledge of porosity does not improve the accuracy of the results.

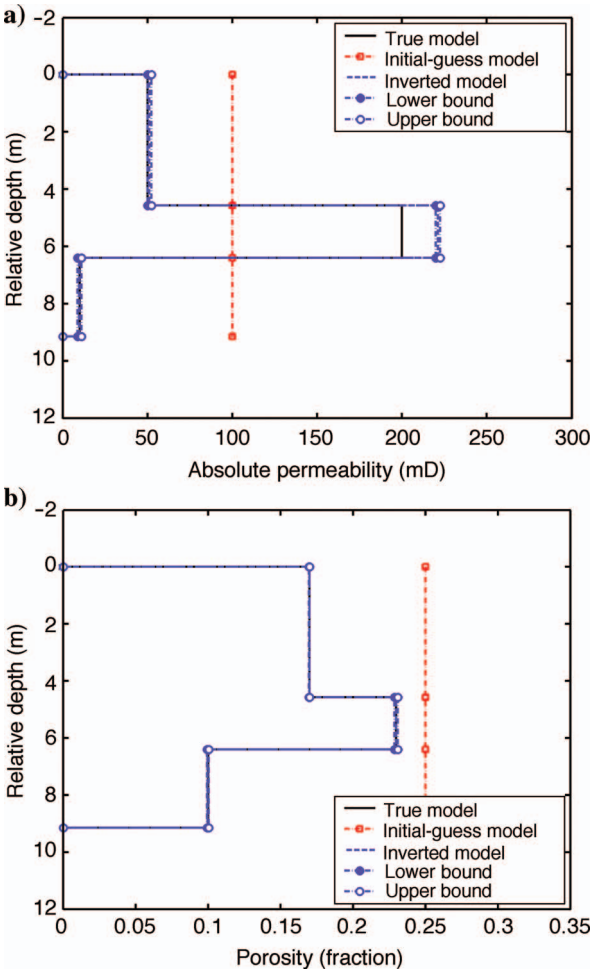

Figure 12. (a) Permeability and (b) porosity values inverted from induction logs acquired with the array-induction imager tool at 12 days after the onset of mud-filtrate invasion. In this example, the numerical grid used for inversion is identical to the one used to generate the synthetic measurements. Inversion results and Cramer-Rao upper and lower uncertainty bounds are shown for the case of measurements contaminated with 3% zero-mean additive Gaussian noise.

Sensitivity of the petrophysical inversion results to uncertainty in a priori information

In the previous section, inversion exercises invoked the assumption that saturation equation parameters, PVT properties of the fluids, and saturation-dependent functions were known a priori from fluid sampling and rock-core laboratory measurements. For a newly discovered hydrocarbon-bearing formation, knowledge of a priori information about saturation equation parameters, PVT properties of fluids, and relative permeability and capillary pressure functions may be limited or uncertain.

The objective here is to quantify the reliability of the petrophysical inversion algorithm with respect to inaccuracies of a priori information. For this purpose, we conduct a systematic sensitivity study in which we invert array-induction logs with perturbed input parameters for saturation equation, viscosity ratio, oleic phase compressibility, saturation-dependent functions, and duration of mud filtrate invasion. We select array-induction logs simulated for the 12th day of mud filtrate invasion, (or equivalently, for the 1.5th day of mud-filtrate invasion with a rate eight times the original invasion rate) for the numerical experiment. Uniform initial-guess values of 100 mD and 25% are assumed for permeability and porosity, respectively. Numerically simulated measurements are contaminated with 1% additive zero-mean Gaussian noise.

Inversions with perturbed saturation equation parameters

We first perform inversions to quantify the sensitivity of inversion results to simultaneous perturbations in Archie's parameters m and n. Figure 14a and b show inversion results for permeability and porosity, respectively, for the perturbed m and n set number one described in Table 3. Similarly, Figure 14c and d display inversion results for the perturbed parameter set number two of Table 3. Finally,

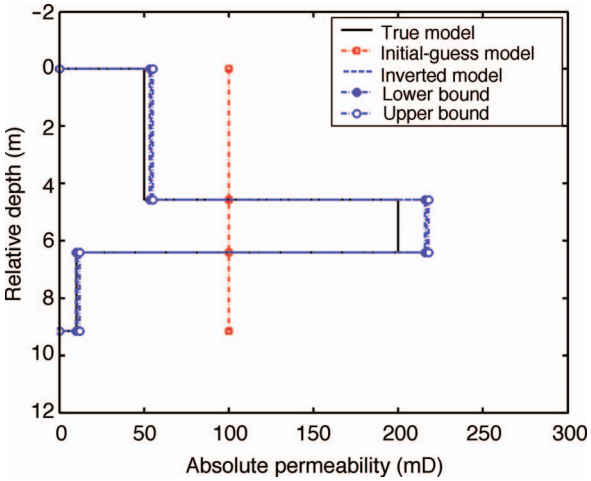

Figure 13. Permeability values inverted from induction logs acquired with the array-induction imager tool 12 days after the onset of mud-filtrate invasion. In this example, the numerical grid used for inversion is identical to the one used to generate the synthetic measurements. Inversion results and Cramer-Rao upper and lower uncertainty bounds are shown for the case of measurements contaminated with 3% zero-mean additive Gaussian noise.

Figure 14e and f show inverted permeability and porosity values, respectively, for the perturbed parameter set number three of Table 3.

In the first test case, we perform a 5% percent positive perturbation on the cementation exponent m, whereas the saturation exponent n is subjected to a 5% negative perturbation. Inversion results indicate that at perturbation levels of 5% of the original parameter (set number one), the petrophysical inversion algorithm yields acceptable values of permeability and porosity. When the magnitude of the perturbation increases to 10% and the sign of the perturbations remain unchanged (set number two), the inverted values do not significantly change from the original model. However, we observe a slight deterioration in the quality of the reconstruction of porosity. For the same perturbation level, a reversal of the sign of the perturbation for n (set number three of Table 3) amplifies the model reconstruction errors for both permeability and porosity. Additional inversion exercises indicate that the inversion yields acceptable reconstructions of permeability and porosity up to a perturbation level of 5%. Above this perturbation level, the quality of the estimated values of permeability deteriorates significantly. Moreover, the quality of the porosity reconstruction is influenced by the perturbation direction which also yields a very undesirable outcome.

Inversions with perturbed oleic phase viscosity and compressibility

Next, we investigate the sensitivity of inversion results to simultaneous perturbations of viscosity ratio and oleic phase compressibility. The objective is to perform petrophysical inversions under the influence of an inaccurate displacement efficiency prescribed for the multiphase fluid-flow forward model. Displacement efficiency is a strong function of the mobility ratio, which is predominantly governed by the ratio of viscosities of the displaced and displacing fluids. In our case, water-base mud filtrate (aqueous phase) displaces the in-situ liquid oil (oleic phase). Therefore, perturbations performed on the oleic phase viscosity can be interpreted as modifications to the displacement efficiency. If the ratio of the viscosity of the displaced fluid with respect to the displacing fluid (μ_o/μ_w) is less than one, then displacement proceeds with a favorable viscosity ratio. If the viscosity ratio is greater than one, displacement takes place with an adverse viscosity ratio. In general, viscosity, density, and compressibility of the fluid phases are interrelated. For instance, high viscosity oils usually exhibit high density and low compress ibility; lighter oils are less viscous and relatively more compressible.

We consider a simultaneous modification of the oleic phase viscosity and compressibility for a given level of oleic-phase density. Figure 15a and b show inversion results for permeability and porosity, respectively, for the perturbed parameter set number one of Table 4. The viscosity ratio for this case is equal to the relatively adverse value of 3.14, as opposed to the actual favorable viscosity ratio of 0.28. Similarly, Figure 15c and d display inversion results for the perturbed parameter set number two of Table 4 where we consider the use of a favorable viscosity ratio of 0.08. Finally, Figure 15e and f show inverted permeability and porosity values, respectively, for the perturbed parameter set number three in Table 4. In this case, we perform inversions by assuming a more adverse viscosity ratio equal to 7.8.

For the investigated cases, inversion results for porosity remain reliable for perturbations of viscosity ratio and oleic-phase compressibility. The inverted permeability values, on the other hand, ex-

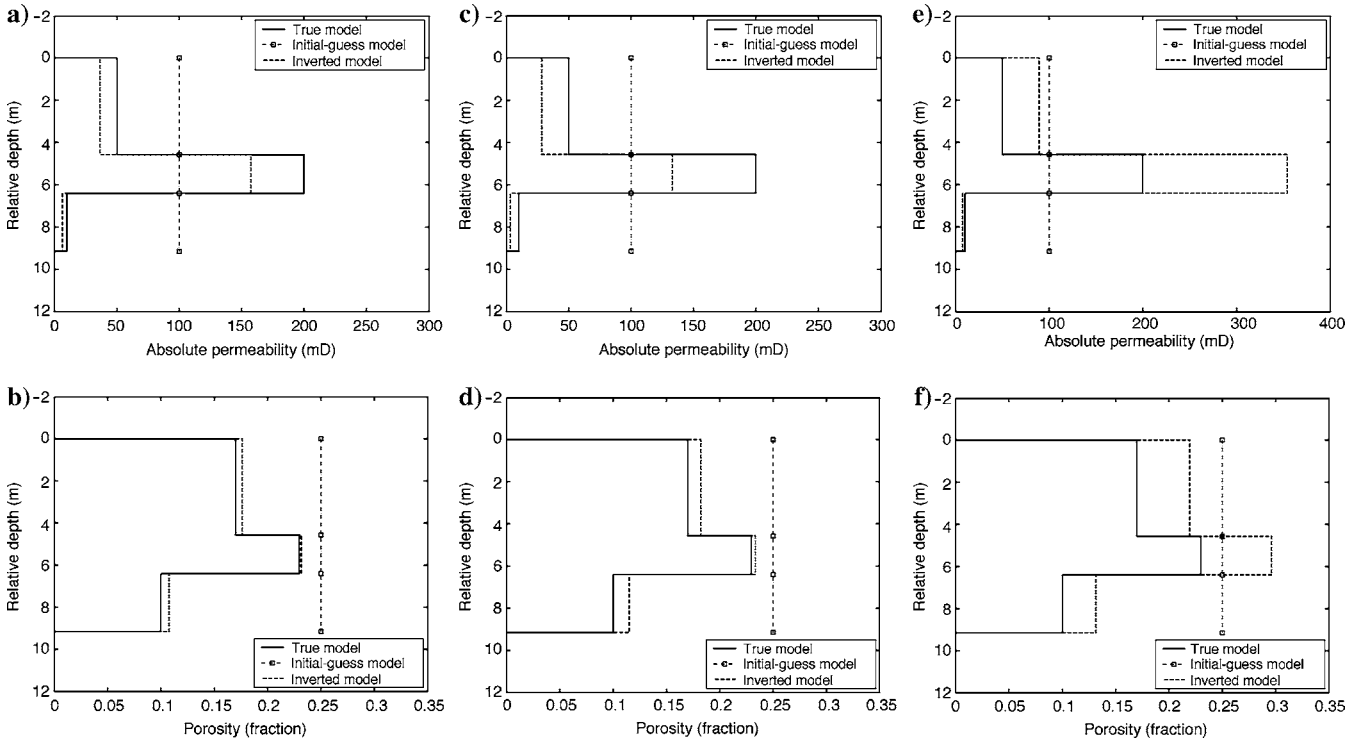

Figure 14. Sensitivity of inversion results to perturbations in Archie's parameters m and n. Panels (a) and (b) show inversion results for permeability and porosity values, respectively, for the perturbed parameter set one shown in Table 3. Panels (c) and (d) show inversion results for permeability and porosity values, respectively, for the perturbed parameter set two listed in Table 3. Panels (e) and (f) show inversion results for permeability and porosity values, respectively, for the perturbed parameter set three listed in Table 3.

hibit limited sensitivity to these perturbations. Overall, the inverted permeability values agree well with the actual permeability values.

Inversions with perturbed saturation-dependent functions

For the synthetic numerical experiments described in this paper, we use parametric relative permeability and capillary pressure functions described independently for each petrophysical layer. The multiphase flow simulator implements these saturation-dependent functions with a modified Brooks-Corey model (Lake, 1989; Semmelbeck et al., 1995) described by the following parametric equations for phase relative permeabilities:

$$S_{wD} = \frac{S_w - S_{wirr}}{1 - S_{wirr} - S_{or}}, \tag{8a}$$

$$k_{rw}(S_{wD}) = k^o_{rw}[S_{wD}]^{e_w}, \tag{8b}$$

and

$$k_{ro}(S_{wD}) = k^o_{ro}[1 - S_{wD}]^{e_o}. \tag{8c}$$

Moreover, the capillary pressure between aqueous and oleic phases is given by

$$P_c(S_{wD}) = P_{ce}[S_{wD}]^{-1/\alpha}. \tag{8d}$$

In the above equations, S_w stands for the saturation of the aqueous phase, and S_{wirr} and S_{or} denote irreducible aqueous and residual oleic phase saturation, respectively. A normalized aqueous phase saturation, S_{wD}, is computed using equation 8a. Saturation-dependent aqueous and oleic phase relative permeability functions, $k_{rw}(S_{wD})$ and $k_{ro}(S_{wD})$, respectively, are computed using end-point aqueous and oleic-phase relative permeabilities k^o_{rw} and k^o_{ro}, and curvature parameters e_w and e_o. On the other hand, the saturation-dependent capillary pressure between oleic and aqueous phases $P_c(S_{wD})$ is parameterized using the entry capillary pressure P_{ce} and the pore-size distribution index α (Semmelbeck et al., 1995). Relative permeability and capillary pressure functions described by equation 8 reflect drainage conditions. Imbibition relative permeabilities are assumed the same as those of drainage. The hysteresis in the saturation-dependent functions is assumed negligible.

In what follows, we quantify the sensitivity of inversion results to perturbations in relative permeability and capillary pressure. Figure 16a and b shows inversion results for permeability and porosity, respectively, obtained by assuming that the relative permeability and capillary pressure functions for all three layers are the same and equal to the ones of layer number 1 in the original (unperturbed) formation model. Figure 16c and d, on the other hand, displays inversion results for permeability and porosity, respectively, obtained by assuming that the relative permeability and capillary pressure func-

Table 3. Parameters of Archie's equation used for the numerical sensitivity study. Note that the parameters included in Archie's equation are dimensionless.

Variable	Actual values	Perturbed set 1	Perturbed set 2	Perturbed set 3
a	1.00	1.00	1.00	1.00
m	2.00	2.10	2.20	2.20
n	2.00	1.90	1.80	2.20

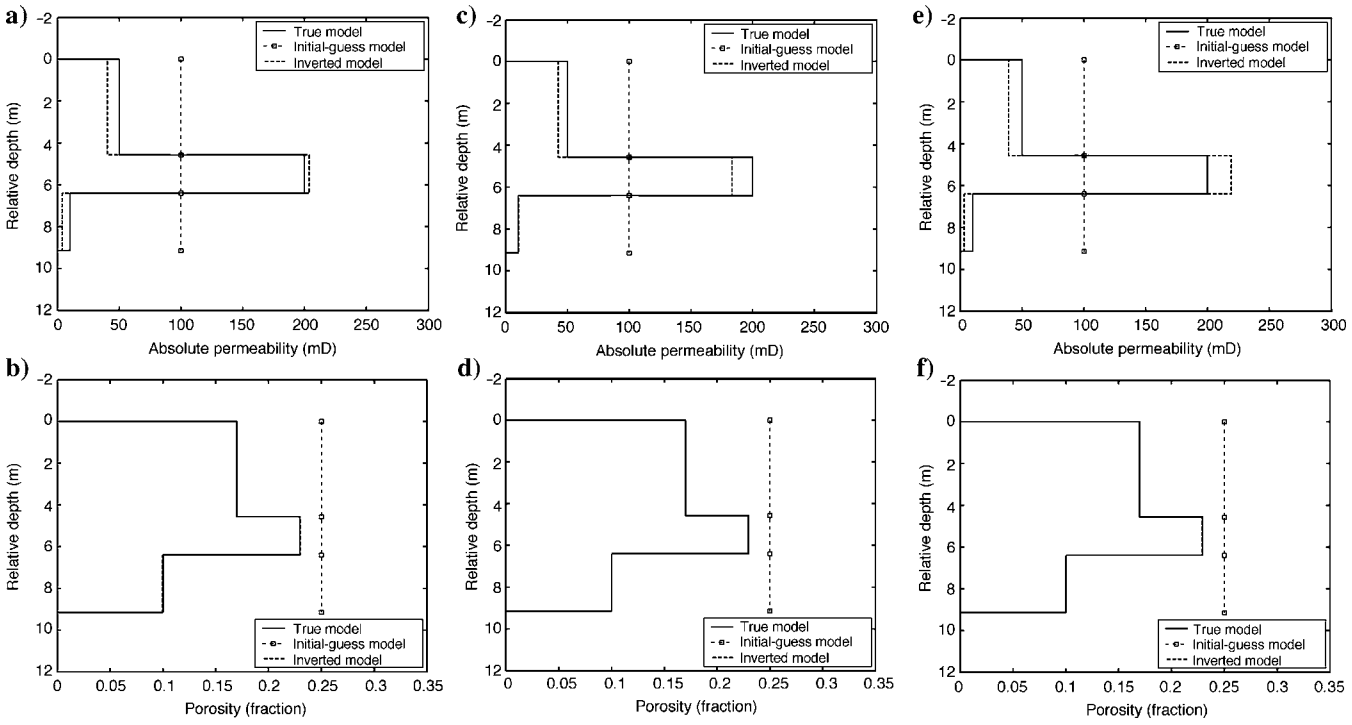

Figure 15. Sensitivity of inversion results to perturbations of viscosity ratio and oleic phase compressibility. Panels (a) and (b) show inversion results for permeability and porosity values, respectively, for the perturbed parameter set 1 shown in Table 4. Panels (c) and (d) show inversion results for permeability and porosity values, respectively, for the perturbed parameter set 2 listed in Table 4. Panels (e) and (f) show inversion results for permeability and porosity values, respectively, for the perturbed parameter set 3 listed in Table 4.

tions for all three layers are the same and equal to the ones of layer number 2 in the original (unperturbed) formation model. Figure 16e and f shows inversion results for permeability and porosity, respectively, obtained by assuming that the relative permeability and capillary pressure functions for all three layers are the same and equal to the ones of layer number 3 in the original (unperturbed) formation model. The sensitivity study is extended using various combinations of the perturbed parameters for saturation-dependent functions. These perturbed parameters are documented in Table 5. Figure 17 and 18 describe the corresponding inversion results for each perturbed set.

We note that inaccuracies on the description of relative permeability and capillary pressure cause the estimated permeability and porosity to deviate from the actual values. In a great majority of the inversions performed with perturbed saturation-dependent functions, inverted porosity values consistently agreed with the true model. On the other hand, the quality of the inverted permeability values appears to be highly case-dependent. Inaccurate descriptions of saturation-dependent functions combined with noisy measurements render the permeability-porosity inverse problem more nonunique when compared to other types of perturbations of a priori information considered in this paper.

Table 4. Oleic phase viscosity and compressibility values used for the numerical sensitivity study.

Variable	Actual values	Perturbed set 1	Perturbed set 2	Perturbed set 3
Compressibility, (kPa^{-1})	2.762×10^{-6}	2.762×10^{-8}	2.762×10^{-4}	2.762×10^{-8}
Viscosity, (Pa.s)	3.550×10^{-4}	4.000×10^{-3}	1.000×10^{-4}	1.000×10^{-2}

Perturbations on the assumed duration of mud-filtrate invasion

We also assess the impact of an error in the estimated time duration of the process of mud-filtrate invasion. This sensitivity study is equivalent to introducing uncertainty on the rate of mud-filtrate invasion because we use a constant time-averaged rate of mud-filtrate invasion. Array-induction logs simulated for the 12th day of mud-filtrate invasion are selected for the numerical experiment. We introduce errors of ±1 day and ±3 days for the assumed duration of mud-filtrate invasion.

Inversion results are shown in Figure 19a and b for a perturbation of +1 day, Figure 19c and d for a perturbation of −1 day, Figure 19e and f for a perturbation of +3 days, and Figure 19g and h for a perturbation of −3 days, respectively. Inversions results indicate that an error of ±1 day in the assumed time of invasion has a marginal effect on the accuracy of the inverted values of permeability and porosity. However, an error of ±3 days in the assumed time of invasion has negative conse-

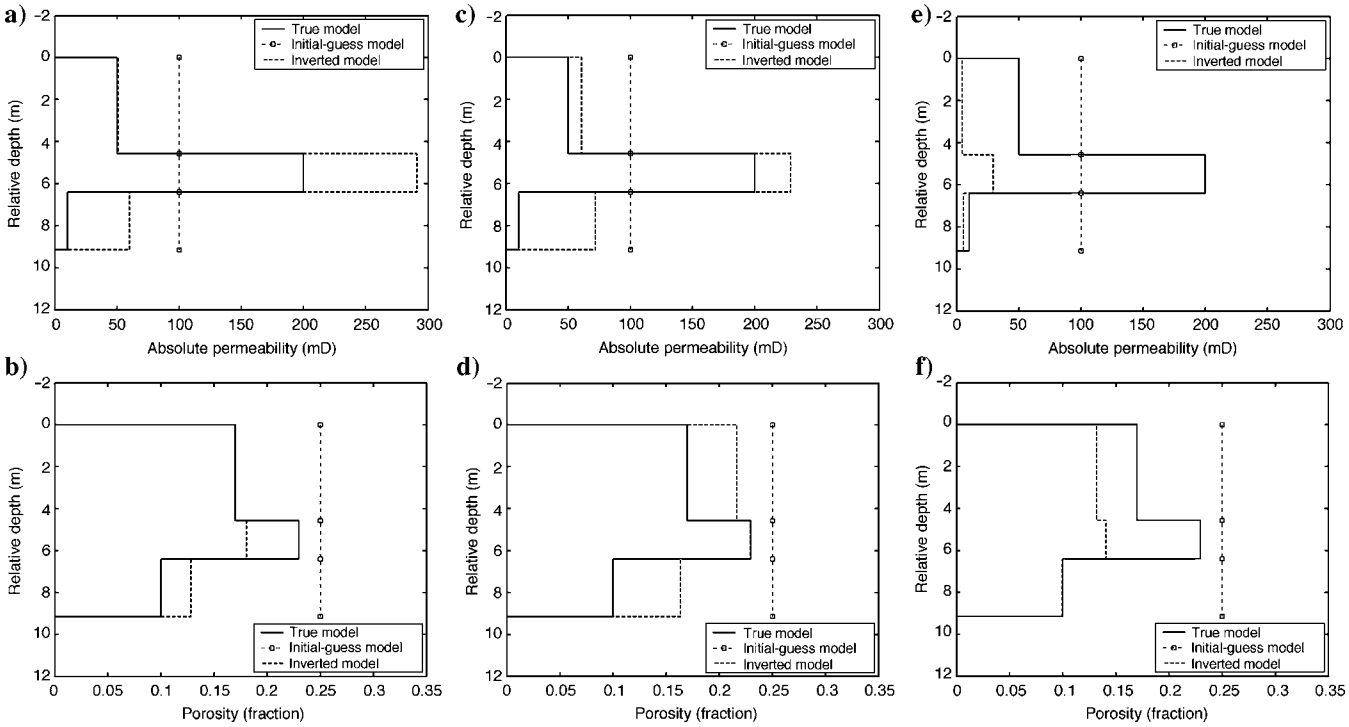

Figure 16. Sensitivity of inversion results to perturbations of relative permeability and capillary pressure. Panels (a) and (b) show inversion results for permeability and porosity, respectively, assuming that the relative permeability and capillary pressure functions for all three layers are the same and equal to the ones of layer number 1 in the original (unperturbed) formation model. Panels (c) and (d) display inversion results for permeability and porosity, respectively, assuming that the relative permeability and capillary pressure functions for all three layers are the same and equal to the ones of layer number 2 in the original (unperturbed) formation model. Panels (e) and (f) show inversion results for permeability and porosity, respectively, assuming that the relative permeability and capillary pressure functions for all three layers are the same and equal to the ones of layer number 3 in the original (unperturbed) formation model.

Table 5. Layer-by-layer modified Brooks-Corey relative permeability and capillary pressure parameters used in the numerical sensitivity study. Note that the parameters S_{wirr}, S_{or}, k^o_{rw}, and k^o_{ro} are reported in fractions. The parameters e_w, e_o, and α are dimensionless.

Layer 1	S_{wirr}	S_{or}	k^o_{rw}	k^o_{ro}	e_w	e_o	P_{ce} (kPa)	α
Actual	**0.350**	**0.150**	**0.150**	**0.600**	**2.750**	**2.500**	**20.684**	**3.000**
Set 1	0.300	0.100	0.100	0.700	2.000	2.000	6.895	1.500
Set 2	0.300	0.100	0.100	0.700	2.750	2.500	20.684	3.000
Set 3	0.400	0.100	0.200	0.550	2.750	2.500	20.684	3.000
Set 4	0.300	0.200	0.100	0.650	2.750	2.500	20.684	3.000
Set 5	0.350	0.150	0.150	0.600	2.750	2.500	10.342	2.500
Layer 2	S_{wirr}	S_{or}	k^o_{rw}	k^o_{ro}	e_w	e_o	P_{ce} (kPa)	α
Actual	**0.275**	**0.200**	**0.200**	**0.550**	**2.250**	**2.000**	**6.895**	**2.000**
Set 1	0.225	0.250	0.250	0.600	2.000	1.850	13.790	1.000
Set 2	0.225	0.250	0.250	0.600	2.250	2.000	6.895	2.000
Set 3	0.325	0.150	0.250	0.500	2.250	2.000	6.895	2.000
Set 4	0.225	0.250	0.150	0.600	2.250	2.000	6.895	2.000
Set 5	0.275	0.200	0.200	0.550	2.250	2.000	13.790	1.500
Layer 3	S_{wirr}	S_{or}	k^o_{rw}	k^o_{ro}	e_w	e_o	P_{ce} (kPa)	α
Actual	**0.450**	**0.100**	**0.100**	**0.750**	**1.750**	**2.750**	**34.474**	**3.500**
Set 1	0.350	0.150	0.150	0.800	1.500	2.500	27.579	2.500
Set 2	0.350	0.150	0.150	0.800	1.750	2.750	34.474	3.500
Set 3	0.500	0.050	0.150	0.700	1.750	2.750	34.474	3.500
Set 4	0.400	0.150	0.050	0.800	1.750	2.750	34.474	3.500
Set 5	0.450	0.100	0.100	0.750	1.750	2.750	17.237	4.000

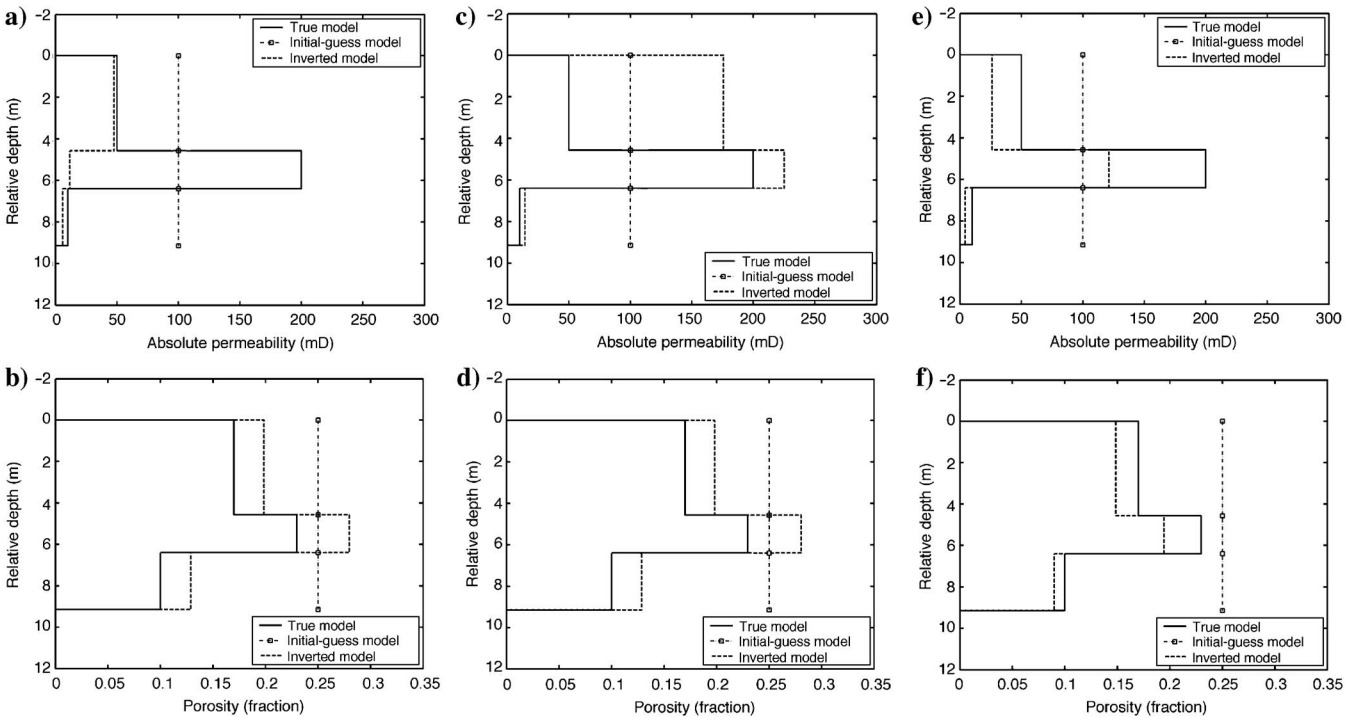

Figure 17. Sensitivity of inversion results to perturbations of relative permeability and capillary pressure. Inversion results for (a) permeability and (b) porosity values for the perturbed parameter set one shown in Table 5. Similar inversion results for perturbed parameter sets two and three are shown in panels (c) and (d) and (e) and (f), respectively.

quences to the accuracy of the inverted values of permeability, while the inverted porosity values remain unscathed.

The outcome of this sensitivity study sheds further light on the validity of the petrophysical inversion technique considered in this paper. Specifically, uncertainty of the duration of invasion time is equivalent to uncertainty in the flow rate of mud-filtrate invasion. The rate of mud-filtrate invasion can be interpreted as a time-varying source condition. This source condition is used to replicate the time evolution of mudcake thickness and mudcake permeability after the onset of invasion. For rock formations with permeabilities greater than $\sim 1 - 5$ mD, laboratory experiments (Dewan and Chenevert, 2001) as well as numerical simulations with INVADE (Wu et al., 2005) show that even though initially the flow rate of mud-filtrate invasion is relatively high (spurt loss of mud filtrate), it quickly asymptotes to a steady state value. For the cases considered in this paper ($k \geq 1 - 5$ mD), the parameters that primarily control the rate of mud-filtrate invasion across mudcake are: mudcake permeability, mudcake thickness, pressure overbalance across mudcake, and viscosity of mud filtrate (Wu et al., 2005). At a given point in time, the volume of mud filtrate that invades the formation is controlled by the product of flow rate of invasion multiplied by the duration of mud-filtrate invasion. Consequently, the analysis of perturbations (errors) of the duration of mud-filtrate invasion on the accuracy of the inverted petrophysical parameters is linearly related to the analysis of perturbations (errors) of parameters that control the rate of mud-filtrate invasion.

Table 6 summarizes equivalent perturbations of the three most important parameters that govern the rate of mud-filtrate invasion with respect to perturbations of the estimated duration of mud-filtrate invasion. Perturbed durations of mud-filtrate invasion are used as reference for this sensitivity study. For each perturbed case (in other words, for each boldfaced row in Table 6), the parameter in each (boldface, nonitalic) column (together with unperturbed estimated duration of mud-filtrate invasion) entails the same volume of mud-filtrate invasion for a given perturbation in the estimated duration of mud-filtrate invasion. In general, we observe that practical perturbations of mudcake permeability, overbalance pressure, and mud-filtrate viscosity do not cause significant variations of the equivalent time of mud-filtrate invasion.

1D inversion of permeability from array-induction logs

For full 1D inversion of array-induction logs, we parameterize the 9.144 m- (30-ft) thick three-layer (geologic layers) formation (shown in Figure 3), into 30 uniform layers of thickness equal to 0.3048 m (1 ft). We assume the availability of porosity values from other ancillary measurements (such as bulk density and neutron logs). Array-induction logs simulated for the 12th day of mud-filtrate invasion, (or equivalently, for the 15th day of mud filtrate invasion with a rate of eight times the original rate of invasion) are selected for this numerical experiment. A uniform initial guess value of 100 mD is assumed for the permeability of all the layers. Array-induction logs were simulated with a 141×30 finite-difference grid and contaminated with 1% and 3% zero-mean additive Gaussian noise. For the inversions, we used a relatively coarser 121×30 numerical grid.

Results for full 1D inversions of permeability are shown in Figure 20. Figure 20a and b show inversion results for cases in which the measurements are contaminated with 1% and 3% zero-mean additive Gaussian noise, respectively. Inversion results indicate a fairly accurate reconstruction of permeabilities for the 1% noise-contamination case. However, for 3% measurement-noise level, the deleterious effect of noise significantly reduces the accuracy of the inverted permeability values.

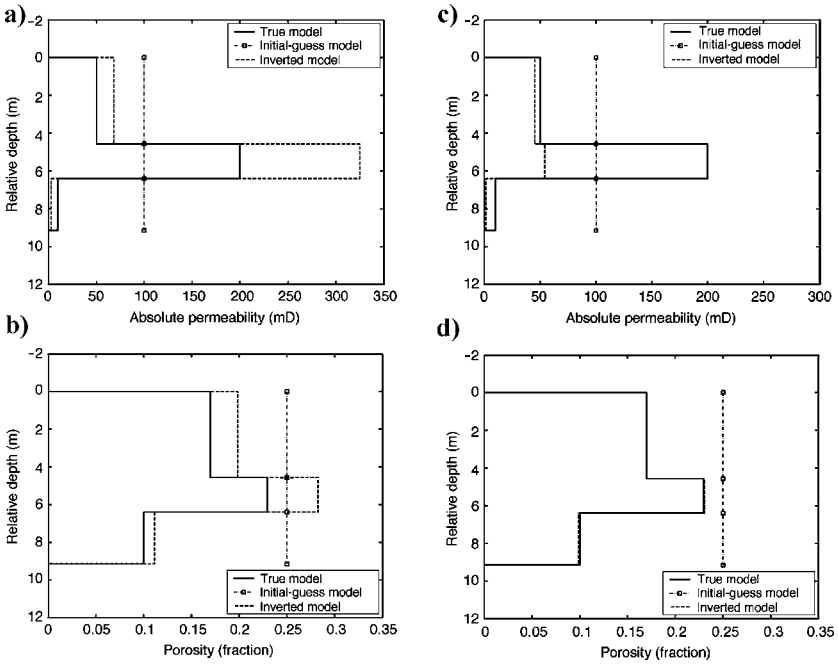

Figure 18. Sensitivity of inversion results to perturbations of relative permeability and capillary pressure. Panels (a) and (b) show inversion results for permeability and porosity values, respectively, for the perturbed parameter set 4 shown in Table 5. Inversion results for the perturbed parameter set 5 are shown in panels (c) and (d).

SUMMARY

Table 1 provides a detailed summary of all the geometrical, mud, and petrophysical parameters assumed in the estimation of porosity and permeability from borehole array-induction logs. In this table, we catalogue the specific source of information used to determine a given parameter, either from a priori information (such as rock-core of PVT fluid measurements) or derived from ancillary measurements. The same table includes a qualitative appraisal of the uncertainty of the estimated values of porosity and permeability resulting from uncertainty of a given assumed parameter. We find that, in general, uncertainties in Archie's and capillary pressure and relative permeability parameters are responsible for the largest error in the estimated values of porosity and permeability.

From this analysis, it follows that porosity, permeability, capillary pressure, and relative permeability have an appreciable influence on the shape of the radial fronts of water saturation and salt concentration resulting from invasion (see, for instance, George et al., 2004). On the other hand, variations of the rate of mud-filtrate invasion (or, equivalently, of the permeability of mudcake and

of the duration of the process of invasion), will uniformly displace the water saturation and salt concentration fronts in the radial direction with marginal influence on the shape of the fronts. The methodology proposed in this paper to estimate permeability relies on the fact that permeability and porosity have the strongest influence on the shape and location of the radial fronts of water saturation and salt concentration. In addition, the inversion methodology proposed in this paper assumes that variations in the location and shape of the radial fronts of water saturation and salt concentration produce measurable variations in apparent conductivity logs that exhibit multiple

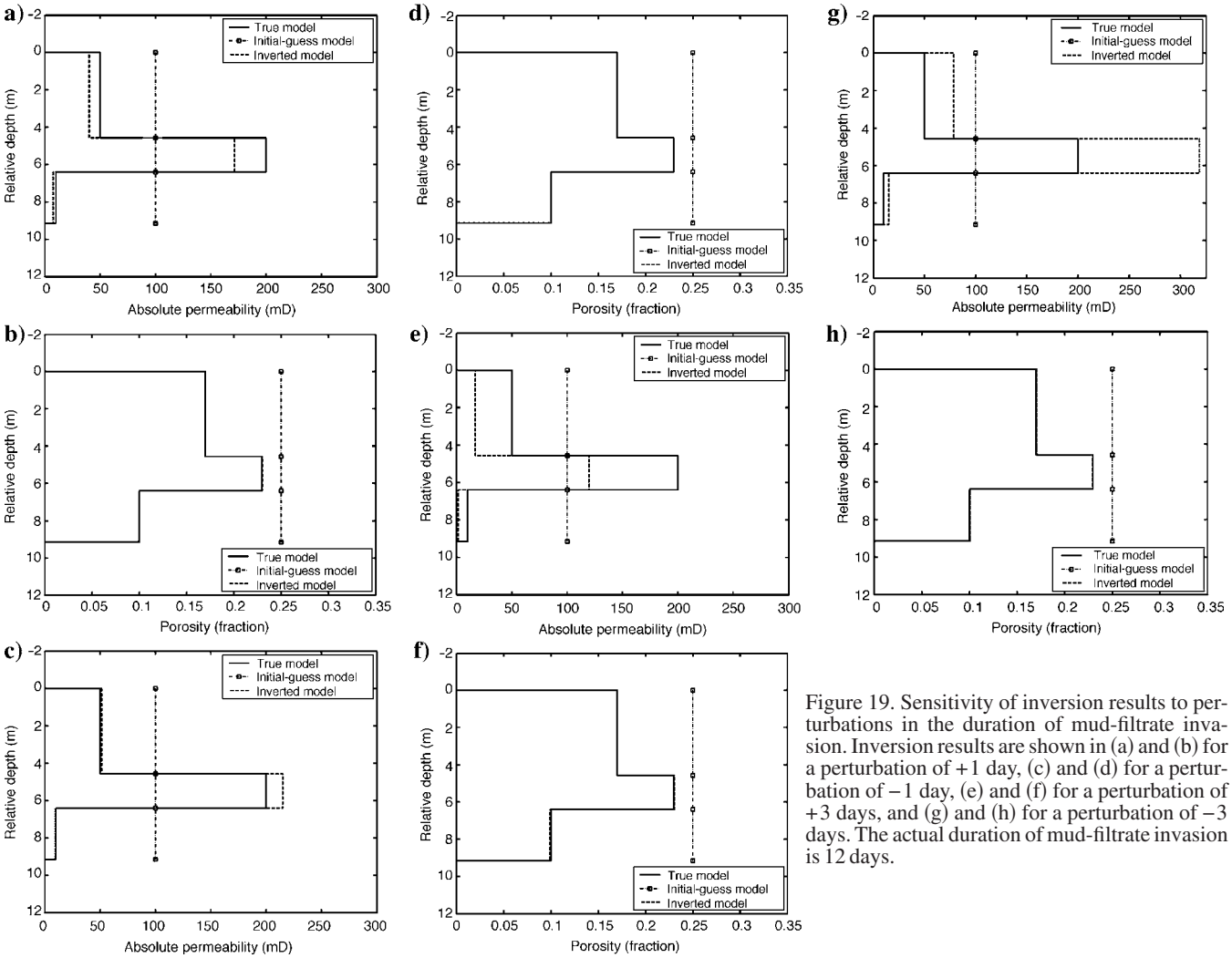

Figure 19. Sensitivity of inversion results to perturbations in the duration of mud-filtrate invasion. Inversion results are shown in (a) and (b) for a perturbation of +1 day, (c) and (d) for a perturbation of −1 day, (e) and (f) for a perturbation of +3 days, and (g) and (h) for a perturbation of −3 days. The actual duration of mud-filtrate invasion is 12 days.

Table 6. List of equivalent perturbations in parameters that govern the rate of mud-filtrate invasion with respect to perturbations in the estimated duration of mud-filtrate invasion.

Case	t (days) (time of invasion)	k_{mc} (mD) (mudcake permeability)	ΔP (MPa) (overbalance pressure)	μ (Pa · s) (mud-filtrate viscosity)
Base	12.00	0.010	4.137	1.274×10^{-3}
Perturbation 1 (+1 day)	13.00	0.011	4.482	1.176×10^{-3}
Perturbation 2 (−1 day)	11.00	0.009	3.792	1.390×10^{-3}
Perturbation 3 (+3 day)	15.00	0.013	5.171	1.019×10^{-3}
Perturbation 4 (−3 day)	9.00	0.008	3.103	1.699×10^{-3}

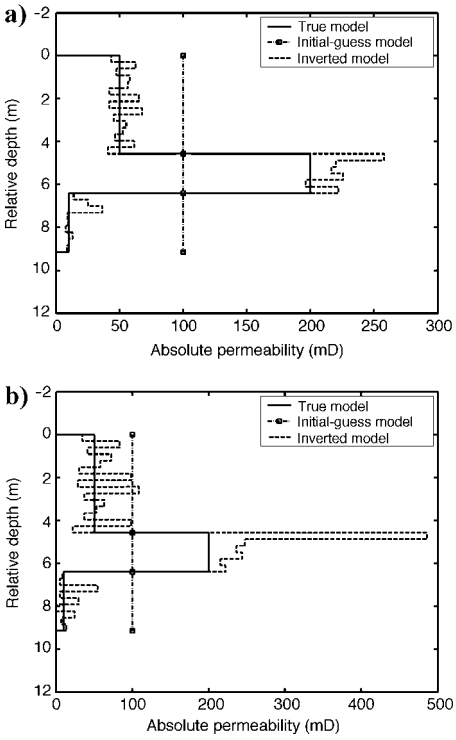

Figure 20. Full 1D inversion of permeability from array-induction logs. Inverted permeability profiles along with true and initial-guess values of permeability for the cases of measurements contaminated with (a) 1% and (b) 3% zero-mean additive Gaussian noise.

radial lengths of investigation. Both marginal differences among the latter logs and invasion beyond the radial length of investigation will cause the inversion methodology proposed in this paper to be unreliable.

Therefore, we recommend that a systematic sensitivity analysis, similar to the one described in this paper, be performed to quantify properly the relative influence of permeability and porosity on induction logs compared to the influence on the same logs as a result of rock-fluid petrophysical properties (e.g., capillary pressure and relative permeability), Archie's parameters, time of invasion, and flow rate of mud-filtrate invasion. Such a sensitivity analysis will assess properly whether porosity and permeability could be estimated reliably and accurately from array-induction logs.

CONCLUSIONS

The synthetic examples described in this paper indicate that array-induction logs can be used to estimate the permeability and porosity of layered rock formations. This estimation is possible because of the physical link that exists between the physics of mud filtrate invasion and the physics of electromagnetic logging. In this paper, the link between porosity, saturation, and electrical conductivity was enforced through Archie's equations, whereas the link between permeability and electrical resistivity was enforced through both Archie's equations and the time evolution of the process of mud-filtrate invasion.

We have shown that array-induction logs in general exhibit a measurable sensitivity to porosity, regardless of the specific petrophysical conditions that govern the process of mud-filtrate invasion. By contrast, the accurate estimation of permeability is controlled largely by a priori information such as mud properties, time of invasion, relative permeability, capillary pressure, fluid viscosity, and initial aqueous phase saturation, among others. Inversion exercises considered in this paper indicated that uncertain knowledge about pressure-volume-temperature dependent properties of the fluids plays a secondary role in the accuracy of the estimated values of permeability and porosity.

Another conclusion is the relative insensitivity of the inversion to acceptable ranges of uncertainty in mud-filtrate invasion parameters such as time of invasion, rate of invasion, and mudcake properties. Uncertainty in Archie's parameters as well as in relative permeability and capillary pressure parameters caused the largest uncertainty in the estimated values of porosity and permeability.

We strongly recommend that the inversion of porosity and permeability from borehole array-induction logs be preceded by a systematic quantitative analysis of the relative sensitivity of induction logs to capillary pressure, relative permeability, initial water saturation, Archie's parameters, time of invasion, and flow rate of mud-filtrate invasion. Only when the sensitivity of the measurements to porosity and permeability is large compared to the sensitivity to other a priori parameters, will the inversion yield reliable and accurate results.

The petrophysical inversion algorithm described in this paper can be used also to estimate spatial distributions of electrical conductivity, which are obtained as a by-product of the inversion of permeability and porosity. However, as opposed to standard algorithms used for the inversion of array-induction logs, the estimated spatial distributions of electrical conductivity described in this paper are consistent with the processes of salt mixing and fluid transport and abide by the law of mass conservation. Given the inherent nonuniqueness of inversion, the enforcement of petrophysical constraints provides a natural way to reduce uncertainty of the estimated spatial distributions of electrical conductivity in the presence of noisy and inadequate array-induction logs.

ACKNOWLEDGMENTS

A note of special gratitude goes to Dr. Steve Arcone, Dr. Tsili Wang, and two anonymous reviewers for their constructive editorial and technical comments. Funding for this work was provided by the University of Texas Austin Research Consortium on Formation Evaluation, jointly sponsored by Anadarko Petroleum Corporation, Baker Atlas, BP, ConocoPhillips, ENI E&P, ExxonMobil, Halliburton Energy Services, Mexican Institute for Petroleum, Occidental Oil and Gas Corporation, Petrobras, Precision Energy Services, Schlumberger, Shell International E&P, Statoil, and TOTAL.

REFERENCES

Archie, G. E., 1942, The electrical resistivity log as an aid in determining some reservoir characteristics: Petroleum Transactions of the American Institute of Mining Engineers, **146**, 54–62.

Aziz, K., and A. Settari, 1979, Petroleum reservoir simulation: Applied Science Publ. Ltd., London.

Barber, T. D., and R. A. Rosthal, 1991, Using a multiarray induction tool to achieve high-resolution logs with minimum environmental effects: Proceedings of the SPE Annual Technical Conference and Exhibition, paper SPE 22725 October 6–9.

Blok, H., and M. Oristaglio, 1995, Wavefield imaging and inversion in electromagnetics and acoustics: Report Et/EM 1995-21, Laboratory of Elec-

tromagnetic Research, Department of Electrical Engineering Centre for Technical Geoscience, Delft University of Technology.
Delshad, M., G. A. Pope, and K. Sepehrnoori, 1996, A compositional simulator for modeling surfactant enhanced aquifer remediation: Journal of Contaminant Hydrology, **23**, 303–327.
Dewan, J. T., and M. E. Chenevert, 2001, A model for filtration of water-base mud during drilling: determination of mudcake parameters: Petrophysics, **42**, 237–250.
Druskin, V., L. Knizhnerman, and P. Lee, 1999, New spectral Lanczos decomposition method for induction modeling in arbitrary 3D geometry: Geophysics, **64**, 701–706.
Dumanoir, J. L., M. P. Tixier, and M. Martin, 1957, Interpretation of the induction-electrical log in fresh mud: Petroleum Transactions of the American Institute of Mining Engineers, **210**, 202–217.
Dussan, V., E. B., B. I. Anderson, and F. M. Auzerais, 1994, Estimating vertical permeability from resistivity logs: Proceedings of the SPWLA 35th Annual Logging Symposium, UU1-UU25.
Epov, M., I. Yeltsov, A. Kashevarov, A. Sobolev, and V. Ulyanov, 2002, Time evolution of the near borehole zone in sandstone reservoir through the time-lapse data of high-frequency electromagnetic logging: Proceedings of the SPWLA 43rd Annual Logging Symposium, ZZ1-ZZ10.
George, B. K., C. Torres-Verdín, M. Delshad, R. Sigal, F. Zouioueche, and B. Anderson, 2004, Assessment of in-situ hydrocarbon saturation in the presence of deep invasion and highly saline connate water: Petrophysics, **45**, 141–156.
Gill, P. E., W. Murray, and M. H. Wright, 1981, Practical optimization: Academic Press Inc.
Habashy, T. M. and A. Abubakar, 2004, A general framework for constrained minimization for the inversion of electromagnetic measurements, Progress in Electromagnetic Research, **46**, 265–312.
Hunka, J. F., T. D. Barber, R. A. Rosthal, G. N. Minerbo, E. A. Head, A. Q. Howard, G. A. Hazen, and R. N. Chandler, 1990, A new resistivity measurement system for deep formation imaging and high-resolution formation evaluation: Proceedings of the SPE Annual Technical Conference and Exhibition, paper SPE 20559.
Lake, L. W., 1989, Enhanced oil recovery, Prentice-Hall, Inc.
Moskow, S., V. Druskin, T. M. Habashy, P. Lee, and S. Davydycheva, 1999, A finite difference scheme for elliptic equations with rough coefficients using a Cartesian grid nonconforming to interfaces: SIAM Journal on Numerical Analysis, **36**, 442–464.
Ramakrishnan, T. S., and D. J. Wilkinson, 1997, Formation producibility and fractional flow curves from radial resistivity variation caused by drilling fluid invasion: Physics of Fluids, **9**, 833–844.
——–, 1999, Water-cut and fractional flow logs from array-induction measurements: SPE Reservoir Evaluation and Engineering, **2**, 85–94.
Semmelbeck, M. E., J. T. Dewan, and S. A. Holditch, 1995, Invasion-based method for estimating permeability from logs: Proceedings of the SPE Annual Technical Conference and Exhibition, paper SPE 30581.
Tobola, D. P., and S. A. Holditch, 1991, Determination of reservoir permeability from repeated induction logging: SPE Formation Evaluation, March, 20–26.
Torres-Verdín, C., and T. M. Habashy, 1994, Rapid 2.5-D forward modeling and inversion via a new nonlinear scattering approximation: Radio Science, **29**, 1051–1079.
Yao, C. Y., and S. A. Holditch, 1996, Reservoir permeability estimation from time-lapse log data: SPE Formation Evaluation, June, 69–74.
Wu, J., C. Torres-Verdín, K. Sepehrnoori, and M. Delshad, 2001, Numerical simulation of mud filtrate invasion in deviated wells: Proceedings of the SPE Annual Technical Conference and Exhibition, paper SPE 71739.
Wu, J., C. Torres-Verdín, K. Sepehrnoori, and M. A. Proett, 2005, The influence of water-base mud properties and petrophysical parameters on mudcake growth, filtrate invasion, and formation pressure: Petrophysics, **46**, 14–32.
Zhang, J-H., Q. Hu, Z.-H. Liu, 1999, Estimation of true formation resistivity and water saturation with a time-lapse induction logging method: The Log Analyst, **40**, 138–148.